Stable behavioral state-specific mesoscale activity patterns in the developing cortex of neonates

Dissertation

zur Erlangung des Grades eines
Doktors der Naturwissenschaften

der Mathematisch-Naturwissenschaftlichen Fakultät
und
der Medizinischen Fakultät
der Eberhard-Karls-Universität Tübingen

vorgelegt
von

Nima Mojtahedi
aus Tabriz, Iran

September 2019

Tag der mündlichen Prüfung: .....

Dekan der Math.-Nat. Fakultät: Prof. Dr. W. Rosenstiel

Dekan der Medizinischen Fakultät: Prof. Dr. I. B. Autenrieth

1. Berichterstatter: Prof. Dr. Olga Garaschuk

2. Berichterstatter: PD. Dr. Gabriele Lohmann

Prüfungskommission: Prof. Dr. Olga Garaschuk

PD. Dr. Gabriele Lohmann

Prof. Dr. Jan Benda

Prof. Dr. / PD Dr. / Dr. .....…

Erklärung / Declaration:

Ich erkläre, dass ich die zur Promotion eingereichte Arbeit mit dem Titel:

„Stable behavioral state-specific mesoscale activity patterns in the developing cortex of neonates“

selbständig verfasst, nur die angegebenen Quellen und Hilfsmittel benutzt und wörtlich oder inhaltlich übernommene Stellen als solche gekennzeichnet habe. Ich versichere an Eides statt, dass diese Angaben wahr sind und dass ich nichts verschwiegen habe. Mir ist be-kannt, dass die falsche Abgabe einer Versicherung an Eides statt mit Freiheitsstrafe bis zu drei Jahren oder mit Geldstrafe bestraft wird.

*I hereby declare that I have produced the work entitled “*Stable behavioral state-specific mesoscale activity patterns in the developing cortex of neonates*”, submitted for the award of a doctorate, on my own (without external help), have used only the sources and aids indicated and have marked passages included from other works, whether verbatim or in content, as such. I swear upon oath that these statements are true and that I have not concealed anything. I am aware that making a false declaration under oath is punishable by a term of imprisonment of up to three years or by a fine.*

Tübingen, den ....

Datum / Date Unterschrift /Signature

Abstract

Endogenous neuronal activity is a hallmark of the developing brain. In rodents a handful of such activities were described in different cortical areas but the unifying macroscopic perspective is still lacking. Here we combined large-scale *in vivo* Ca^{2+} imaging of the dorsal cortex in naturally behaving neonatal mice with advanced mathematical analyses to reveal unique behavioral state-specific maps of endogenous activity. These maps were remarkably stable over time within and across experiments, and used patches of correlated activity with little hemispheric symmetry as well as stationary and propagating waves as building blocks. Importantly, the maps recorded during motion and rest were almost inverse, with sensory-motor areas active during motion and posterior-lateral areas active at rest. The retrosplenial cortex engaged in both resting- and motion-related activities, building functional long-range connections with respective cortical areas. Together, these data provide so far the most complete view on the endogenous network activity pacing development of cortex-wide functional networks in neonates.

Keywords: endogenous network activity, large-scale *in vivo* Ca^{2+} imaging, state-specific activity maps, stationary waves, propagating waves, functional long-range connections.

Zusammenfassung

Endogene neuronale Aktivität ist ein Markenzeichen des sich entwickelnden Gehirns. Bei Nagetieren wurden einige solcher Aktivitätsmuster in verschiedenen kortikalen Bereichen beschrieben, aber eine einheitliche makroskopische Perspektive fehlt noch. Hier kombinierten wir großflächige in vivo Ca^{2+}-Bildgebung des dorsalen Kortex in natürlich verhaltenden neonatalen Mäusen mit erweiterten mathematischen Analysen, um zustandsspezifische Karten der endogenen Aktivität zu erhalten. Diese Karten waren innerhalb und zwischen den Experimenten bemerkenswert stabil und setzten sich aus Bereichen mit korrelierter Aktivität geringer hemisphärischer Symmetrie sowie stationären und sich ausbreitenden Wellen zusammen. Interessanterweise waren die Karten, die während der Bewegung und in Ruhe aufgezeichnet wurden, fast invers, mit sensorisch-motorischen Bereichen, die während der Bewegung aktiv waren, und posterior-lateralen Bereichen, die in Ruhe aktiv waren. Der retrospleniale Kortex beteiligte sich sowohl an Aktivitäten während in Ruhe als auch während der Bewegung und bildete funktionelle Langstreckenverbindungen zu den jeweiligen kortikalen Bereichen. Zusammengenommen bieten diese Daten den bisher vollständigsten Überblick über die endogene Netzwerkaktivität, die die Entwicklung kortikaler funktioneller Netzwerke bei Neugeborenen vorantreibt.

Schlüsselwörter: endogene Netzwerkaktivität, großflächige in vivo Ca^{2+}-Bildgebung, zustandsabhängige Aktivitätskarten, stationäre Wellen, ausbreitende Wellen, funktionale Langstreckenverbindungen.

Acknowledgements

First of all, I would like to express my sincere gratitude to my first supervisor Prof. Dr. Olga Garaschuk for all her supports and helps during my PhD study.

Besides, I would like to thank the other members of thesis committee: Prof. Dr. Matthias Bethge, Prof. Dr. Jan Benda and PD. Dr. Gabriele Lohmann for their wise advices and criticisms.

My thanks also go to Dr. Yury Kovalchuk for his technical and experimental helps and our technicians Ms. Andrea Weible and Ms. Elizabeta Zirdum for their helps for experiment preparation.

I have to thank my collaborator Alexander Böttcher and all colleagues in the Neurophysiology department.

Big thanks to my parents for all their whole life supports which without them doing PhD for me was not possible.

Last but not least, I would especially like to thank my wife Marjan for her love and extreme support, for being with me in difficult situations and being my best friend in each moment of my life.

Table of contents

List of abbreviations

CNS	central nervous system
Ca^{2+}	calcium
SPAs	synchronous plateau assemblies
cENO	cortical early network oscillation
AMPA	α-amino-3-hydroxy-5-methyl-4-isoxazolepropionic acid
NMDA	N-Methyl-D-aspartic acid
GABA	gamma-Aminobutyric acid
GDPs	giant depolarizing potentials
SC	superior colliculus
LGN	lateral geniculate nucleus
V1	area in the visual cortex
EGO	early gamma oscillation
SGNs	spiral ganglion neurons
IHC	inner hair cells
S1	area in somatosensory cortex
M1	area in motor cortex
EEG	electroencephalography
MRI	magnetic resonance imaging
CT	computed tomography
PET	positron emission tomography
MEG	magnetoencephalography
HMM	hidden markov model
ROI	region of interest
PCA	principal component analysis
ICA	independent component analysis
NMF	nonnegative matrix factorization
DBN	dynamic bayesian network

IR	infrared
EMG	electromyography
UV	ultraviolet
FWHM	full width at half maximum
ΔF/F	relative changes in fluorescence
MSSA	multi-channel singular spectrum analysis
IQR	interquartile range
Au	auditory cortex
AU	arbitrary unit

List of figures

Introduction

Brain development

The brain is a sophisticated organ in all vertebrates that plays a crucial role in the body. In humans, this organ has several main functions such as processing sensory information, regulating blood pressure and breathing, controlling the release of hormones, etc. To do information processing the brain requires rich structures that do proper computation of incoming information in a reasonable time. Considering brain size and structure in embryo reveals that it needs the stringent developmental procedure (Figure 1). This strict developmental process has to be organized in a spatiotemporal manner to build up an intricate brain structure.

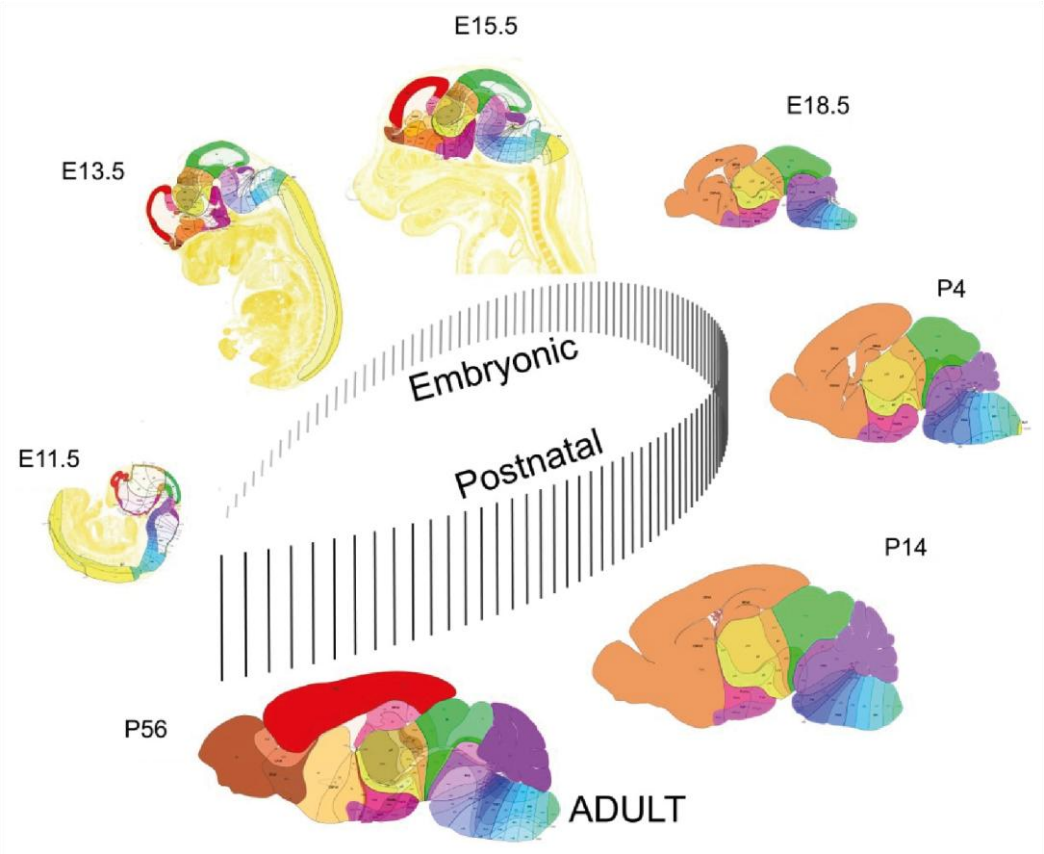

Figure 1. Developing mouse brain.
Taken from Allen et al., 2010**.**

In humans and many other mammalian species, the brain dynamically goes through different developmental stages that begin before the birth and, depending on species, continue after adolescence (B. L. Finlay & R. B. Darlington, 1995; Tau & Peterson, 2010). Genetic factors, as well as environmental inputs, play essential roles in the process of brain maturation. In general, brain development can be divided into three phases; (i) prenatal activity-independent period, (ii) prenatal activity-dependent period and (iii) postnatal activity-dependent period. In rodents, during embryonic development (early prenatal days), genetic factors govern the establishment of connections in immature neural circuits. In the second phase during late prenatal and early postnatal days, experience-independent intrinsic activities interact with genetic factors to orchestrate the development of the brain structures. During the third phase, brain development mainly relies on neural network activities caused by the interaction of the brain with environmental inputs (Hanganu-Opatz, 2010; Rustem Khazipov & Luhmann, 2006; Manley, 2013; Spitzer, 2006; Tierney & Nelson, 2009). Furthermore, several studies have shown that such correlated neuronal activities are present in many regions of the developing central nervous system (CNS) (Adelsberger, Garaschuk, & Konnerth, 2005; O Garaschuk, Linn, Eilers, & Konnerth, 2000; Hanganu, Ben-Ari, & Khazipov, 2006; Rustem Khazipov et al., 2004; Luhmann & Khazipov, 2017).

In the rodent forebrain many of the initial coarse connections are refined during the first postnatal week in an experience-independent manner leading, for example, to the eye-specific input segregation in the lateral geniculate nucleus of the thalamus and formation of the retinotopic map in the visual (Ackman & Crair, 2014a; Kirkby, Sack, Firl, & Feller, 2013) or the emergence of the barrel map in the somatosensory (Luhmann, Sinning, Yang, & Reyes-puerta, 2016; C. C. H. Petersen, 2007) cortex. Because during this period, activation of these cortices through extrinsic (sensory)

stimuli is rather limited (see figure. 2 in ref. (Hanganu-Opatz, 2010)), this refinement likely relies on intrinsic neuronal activity. Such intrinsic activities have been found in multiple brain regions and were shown to have distinct spatiotemporal properties.

During rodent embryonic development, cortical activities are mostly uncorrelated and occur either as calcium fluctuations or as electrically-driven Ca^{2+} spikes (Allene et al., 2008; Owens & Kriegstein, 1998). At birth, cortical activities show more coherent behavior mainly relying on gap junction-mediated electrical activity (Kandler & Katz, 1998; Yuste, Nelson, Rubin, & Katz, 1995). Ca^{2+} imaging, combined with electrophysiological recordings, revealed that the interactions between a small group of cells connected via gap junctions results in spontaneous synchronized Ca^{2+} plateaus (Crépel et al., 2007). In brain slices, SPAs (synchronous plateau assemblies) were shown to occur mainly at birth and during early postnatal development. They are spatially restricted and do not show propagating behavior.

Large-scale oscillatory calcium waves called cortical early network oscillations (cENO), has been originally found in slices of one- to four-day-old (P1–P4) rats using imaging techniques (O Garaschuk et al., 2000). The cENOs are synaptically-driven and propagate in a wave-like fashion, usually starting posteriorly in the entorhinal/temporal cortex and propagating towards the perirhinal/insular cortex with a mean speed of 2.1 mm/sec. Their initiation depends on the activation of AMPA and NMDA receptors and a developmental shift of GABAergic transmission from depolarizing to hyperpolarizing stopped the cENOs. The cENO-like activity was also reported in vivo, in the temporal cortex of non-anesthetized mice. These endogenous Ca^{2+} waves are expressed mainly during sleep-like resting states and disappeared during the animal's movement (Adelsberger et al., 2005). Another type of synaptically-driven activity has been

described in rat slices from the hippocampal area using electrophysiology(YEHEZKEL BEN-ARI, ENRICO CHERUBINI, 1989). In slices, these spontaneous giant depolarizing potentials (GDPs) were observed in the majority of neurons during the first postnatal days.

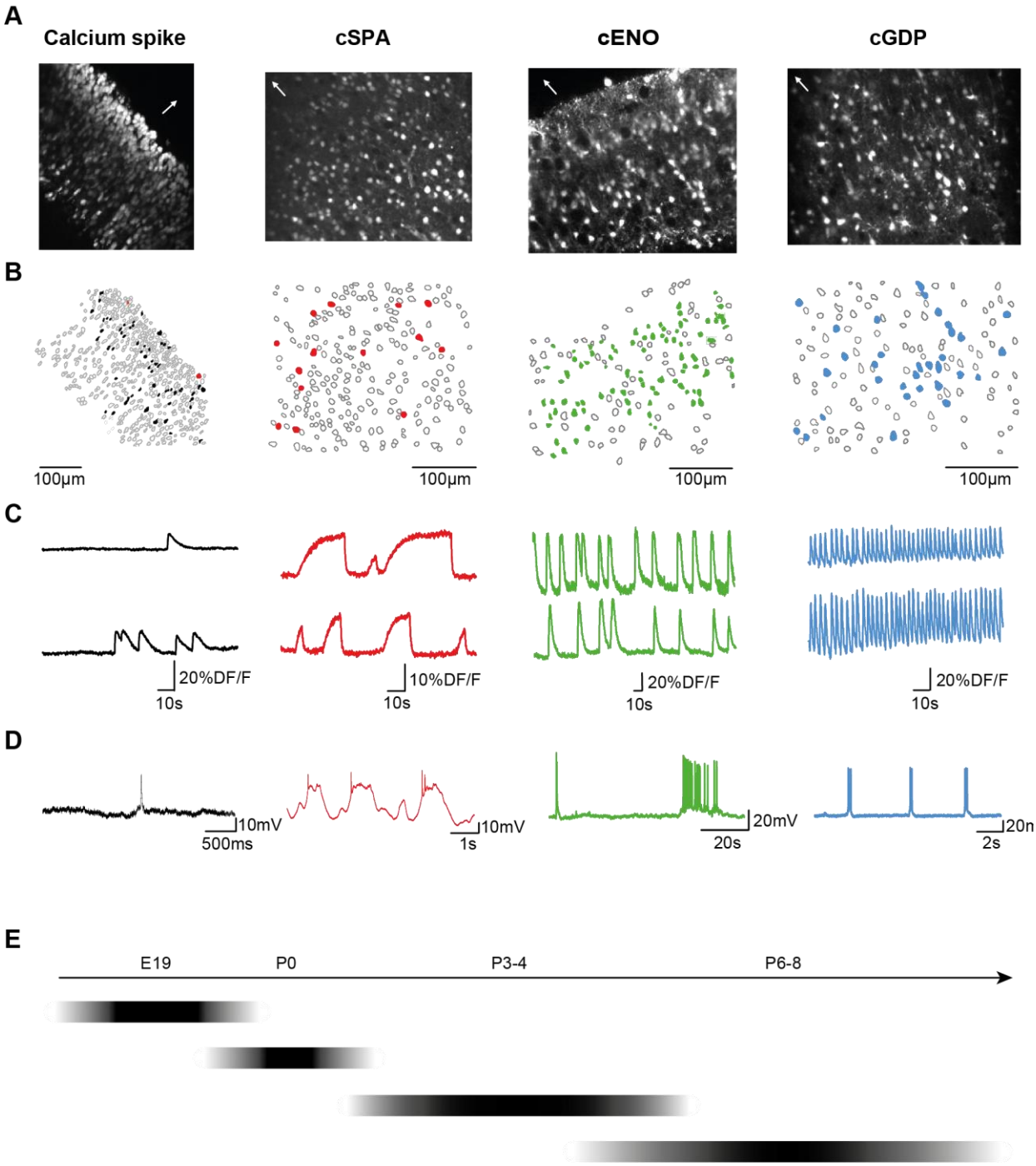

Figure 2. Spontaneous neuronal activities during development.
The figure is taken and modified from, Allene et al., 2008.

The strength of this transient type of activity decreased during development (from day 9 on) and GDPs disappeared around P12 (postnatal day 12). GDPs critically relied on the depolarizing GABAergic transmission and were shown to be generated by a localized population of the interneurons in the layer CA3 of the hippocampus. It remains, however, unclear whether depolarizing GABAergic transmission represents a genuine feature of the developing brain rather than an artifact of tissue slicing, as it was not present in an in vivo cortex but was readily seen after preparing tissue slices including the same cells, previously studied in vivo (Kirmse et al., 2015).

Extracellular multielectrode recordings in the in vivo somatosensory cortex of P0-P7 rats revealed three synchronized oscillatory activity patterns: spindle bursts, gamma oscillations, and long oscillations (J.-W. Yang, Hanganu-Opatz, Sun, & Luhmann, 2009). The data showed that spindle bursts and gamma oscillations are restricted to local neuronal networks. Long oscillations, however, were able to propagate over the large areas.

Considering different spatiotemporal activity patterns in early development described above, it is interesting to see how they modulate brain circuits. Intrinsic non-evoked activities have been reported in the neocortex (Adelsberger et al., 2005; Corlew, Bosma, & Moody, 2004; O Garaschuk et al., 2000; Luhmann et al., 2016), hippocampus (Olga Garaschuk, Hanse, & Konnerth, 1998; Villette et al., 2016; YEHEZKEL BEN-ARI, ENRICO CHERUBINI, 1989) area, and in the sensory cortices such as visual (Ackman & Crair, 2014b; Blumberg, 2010; Galli & Maffei, 1988; Hanganu et al., 2006; Rochefort et al., 2009), auditory (Clause et al., 2014; Tritsch, Yi, Gale, Glowatzki, & Bergles, 2007) and somatosensory (Blumberg, 2010; Rustem Khazipov et al., 2004; Luhmann & Khazipov, 2017; Minlebaev, Ben-Ari, & Khazipov, 2009). In the visual system of the rodents, because eyes are closed after

birth, all activities during early postnatal days are intrinsic. Simultaneous in vivo recording of the retina, midbrain and the visual cortex in neonatal mice suggested that spontaneous waves generated in the retina propagate through the superior colliculus (SC) and the lateral geniculate nucleus (LGN) to V1 area in the visual cortex thus suggesting modulatory effect of this activity on the visual system circuitry (Badalà, Nouri-mahdavi, & Raoof, 2012; Triplett et al., 2009). Moreover, it was shown that the retinal waves play a crucial role for the formation of the retinotopic map, eye-specific input segregation, and orientation tuning of V1 neurons (Ko et al., 2013; Rochefort et al., 2011; S. L. Smith & Trachtenberg, 2007). In vivo two-photon Ca^{2+} imaging of the developing visual cortex revealed two independent activity patterns potentially able to modulate the V1 circuitry: the synchronized network activity driven by gap junctions and the retinal waves. Whereas the frequency of gap junctions-driven events decreases with age, the rate of cortical events driven by retinal waves increased (Siegel, Heimel, Peters, & Lohmann, 2012). In general, in mice the frequency of the Ca^{2+} waves in the visual cortex increases gradually during development and at the end of the second postnatal week, right before eye-opening, these waves engage a significant fraction of neurons. Eye-opening however, causes a desynchronization of this activity (Rochefort et al., 2009). Thus, with eye opening the spontaneous activity in the V1 becomes sparser and less synchronized.

In the somatosensory cortex, maturation occurs earlier than in the visual system. Focusing on the barrel cortex, formation of the barrel map starts at birth, and the initial activity-dependent refinement of the network happens during early postnatal days (Rakic, 1976; Rakic, Ayoub, Breunig, & Dominguez, 2009). In vitro, slow oscillatory cENO-like activity is typical for the somatosensory cortex. As explained above, this activity propagates slowly and covers large cortical areas (Allene et al.,

2008; O Garaschuk et al., 2000). Additionally, electrical in vivo recordings identified early gamma oscillations (EGOs) and spindle bursts as the principal activity patterns in the barrel cortex (R. Khazipov, Minlebaev, & Valeeva, 2013; Luhmann, 2016). EGOs are different from adult gamma oscillations. They occur during early postnatal days and disappear after P7-P8. In contrast, adult gamma oscillations start after P13. The major difference between these two activity patterns is their spatial organization. EGOs are restricted to single cortical columns but adult gamma oscillations have both local and long-range synchronization (R. Khazipov et al., 2013). Besides, the area activated by spindle bursts is larger and the duration is longer compared to EGOs (J.-W. Yang et al., 2009). Whereas generation of EGOs is highly dependent on excitatory inputs from the thalamus (J. W. Yang et al., 2013), the mechanisms underlying the generation of spindle bursts are not well understood. However, there is an evidence suggesting that spindle bursts during early development are generated differently than adult's sleep spindles (McCormick, Trent, & Ramoa, 1995). Eliminating spindle bursts by selectively removal of subplate neurons (Tolner, Sheikh, Yukin, Kaila, & Kanold, 2012) shows the savior effect on the development of cortical circuitry and suggests the critical role of this type of activity for the formation of cortical architecture. Furthermore, EGOs are important for topographically aligned thalamocortical connections (R. Khazipov et al., 2013).

Similar to other cortical areas, spontaneous activity has been reported in the auditory system before the onset of hearing (Dimitrova et al., 2017b; Lippe, 1994; Sonntag, Englitz, Kopp-Scheinpflug, & Rubsamen, 2009). It has been suggested that this rhythmic activity starts in the cochlea (Dimitrova et al., 2017b; Lippe, 1994) and promotes maturation of the auditory circuitry (Dimitrova et al., 2017a; Glueckert et al., 2003; Mostafapour, Cochran, Mae Del Puerto, & Rubel, 2000) or tuning of the

tonotopic map (Kandler, Clause, & Noh, 2009). This activity is likely initiated in the inner hair cells (IHC), which can produce Ca^{2+} spikes before the onset of hearing (Corne´J. Kros, 2004) and cause Ca^{2+}-mediated glutamate release (Beutner & Moser, 2001; Glowatzki & Fuchs, 2002; Johnson, Marcotti, & Kros, 2005). This glutamate release activates spiral ganglion neurons (SGNs). In these neurons, NMDA receptors were shown to boost the cell's spiking rate and increase neuronal participation in each wave of spontaneous activity (YingXin Zhang-Hooks, Amit Agarwal, Masayoshi Mishina, & Dwight E. Bergles, 2016). Thus, the rhythmic firing pattern triggered by the IHC travels through the SGNs to various auditory centers of the brain (Wang et al., 2015). The functional role of the spontaneous activity for the development of the auditory system has been shown by manipulating (such as cochlea ablation or disrupting in neurotransmitter release) occurrence of such activities in the cochlea. Any manipulation on the cochlea or the IHC cause savior changes in the SGNs and in the brain such as degeneration of afferent fibers or apoptotic death of neurons (Glueckert et al., 2003; Hirtz et al., 2011; Mostafapour et al., 2000). In general, the maturation of the auditory system is governed by sequential developmental steps. Before the onset of hearing, in rodent around P11, no evoked responses are detected in the auditory cortex (Geal-Dor, Freeman, Li, & Sohmer, 1993). However, from P11-P12 on a small region start to show response to mid-range frequencies (de Villers-Sidani, Chang, Bao, & Merzenich, 2007). Moreover, spike latency reported for the developing auditory cortex is in the range of 20-40 ms (de Villers-Sidani et al., 2007). This value decreases for adult's AI reaching the value of 5-20 ms(Kelly & Sally, 1988; Polley, Read, Storace, & Merzenich, 2007)

In summary, early development of the brain, which starts with proliferation and migration of cells and continues with dendritic and axonal extension and network

refinement, is driven by highly sophisticated and hierarchic patterns of endogenous activity. Activity-dependent maturation contains two stages: (i) experience-independent, relying mainly on intrinsic activity patterns and (ii) experience-dependent, mainly driven by external stimuli. Intrinsic (spontaneous) activity patterns were seen in many brain regions and belong, in general, to three distinct types. The first type is represented by intrinsic asynchronized single cell activities which are seen during early, largely embryonic, development. This type is followed by a spontaneous activity synchronized among a small population of neurons. These synchronously active cells are often connected through the gap junctions. Next, the chemical synapses form and become involved, creating large-scale network bursts and waves. The synaptically-driven spontaneous network activities in some cortical regions (e.g., prefrontal, motor or somatosensory cortex) were reported to be entrained by the activity in the other cortical/subcortical structures (e.g. hippocampus, S1, thalamus or M1, respectively) likely priming the functional coupling between the two areas seen in the adulthood (An, Kilb, & Luhmann, 2014; Antón-Bolaños et al., 2019; Brockmann, Pöschel, Cichon, & Hanganu-Opatz, 2011). It seems that during development spontaneous activity starts on a micro-scale and continues on a macro-scale thus contributing to formation of large scale neural networks.

Neuroimaging

Studying a complex organ like the brain requires monitoring techniques that capture the structural and functional information of that organ. Variety of methods have been introduced for studying the brain function and, in general, these techniques can be classified into the electrophysiological recording and imaging techniques.

Electrophysiological recordings measure the electrical signals from single cells or populations of cells at a high temporal resolution to understand the electrical properties of the tissue under study and to detect the occurrence of action potentials (Narahashi, 2004). Intracellular or extracellular recordings, despite their high temporal resolution, are limited to a small and, moreover, undefined area. However, there are several extensions, such as multielectrode arrays or electroencephalography (EEG), which increased spatial range of the recordings but not their spatial resolution.

In addition, different imaging techniques are widely used for brain monitoring to capture both structural and functional information. They are divided into few categories based on their technology and application. Among popular imaging techniques, one can name single- and two-photon microscopy, Magnetic Resonance Imaging (MRI), Computed Tomography (CT), and Positron Emission Tomography (PET).

MRI is a non-invasive 3D imaging technique with several clinical applications. This technique, with its extensions, creates the anatomical and functional images of the living organ at a mid-level spatial and temporal resolution (Grover et al., 2015). CT is another 3D imaging technique with higher spatial resolution in comparison to the MRI. This technique is economically cheaper and the images are obtained faster than with the MRI. However, CT provides only structural information and the safety level, depending on the application, is much lower than with the MRI. Due to the ionizing radiation used in the CT, it is not a proper imaging technique for experimental studies (Ginat & Gupta, 2014). PET is a minimally invasive technique with poor spatial resolution. Its working principle is based on the radioactive substances and the PET is generally used to monitor metabolic processes.

EEG, MEG, fMRI, and PET, despite their poor spatial and/or temporal resolution, non-invasively measure the activity of an enormous number of cells and therefore became popular recording techniques in the human studies (Paans, 2004).

Instead of using radiation or radioactive substances, optical techniques use the light for monitoring a single cell or population of cells as well as their structures. Fluorescence microscopy is an optical recording method, and its principle is based on collecting the light emitted by the excited fluorophores (Sanderson, Smith, Parker, & Bootman, 2014). Simply speaking, the excitation light sent from the light source is absorbed by the fluorophore substance. In return, the substance emits light of a specific wavelength which is filtered and then detected by the camera.

Due to its noninvasive nature, fluorescence microscopy is an essential tool in biology. The use of multiple fluorophores makes it possible to observe complex structures simultaneously. Spatial and temporal resolution, as well as image depth, are the major factors to be considered when choosing which type of fluorescence microscopy to use.

For visualization of dynamical processes in the living cells, one has to use fluorophores able to monitor the activity of the cell. In the nerves system, changes in the intracellular Ca^{2+} concentration are involved in and often trigger many cellular processes (Neher & Sakaba, 2008; Zucker, 1999). Thus, investigating cell's Ca^{2+} signaling gives an insight into the cell function. Ca^{2+} imaging represents a recording technique using fluorescent Ca^{2+} indicators for monitoring changes in the intracellular Ca^{2+} concentration. Ca^{2+} indicators used nowadays divided into chemical and genetically-encoded indicators (for review, please see (Grienberger & Konnerth, 2012)).

Taking all, imaging techniques provide multi-dimensional data in a less invasive way. Besides, Ca^{2+} imaging has a unique capability in presenting complex structural and functional aspects of the cell.

Data analysis

Above we briefly introduced advanced technologies and how they allow studying cellular structures and functions. While this remarkable capability facilitates investigating complex organs like the brain, they produce an enormous amount of data and cause new challenges to analyze them. In the case of Ca^{2+} imaging, fluorescence intensity is captured at a given sampling rate over a single neuron or population ensemble. Since the captured intensity reflects neuronal activity, the aim is first to extract the fluorescence intensity in each neuron. To do that, each neuron must be spatially segmented, and the average intensity in a given segment needs to be calculated over time. The basic approach to this task is based on the time-consuming manual segmentation of each neuron in a given spatiotemporal data set. As long as the dataset contains only a small number of neurons, the manual segmentation is applicable. In the large-scale recording, when the field of view contains a population of neurons, automatic or semi-automatic approach is a necessity.

Considering the size of the neuron, any small spatial shift during the data acquisition affects the recorded fluorescence intensity. To solve this problem, as a preprocessing step, an artifact from motion needs to be removed. To do that, several algorithms have been published such as Hidden Markov Model (HMM) approach (Dombeck, 2007), hill-climbing method (Lucas & Kanade, 1981), subpixel registration (Thévenaz, Ruttimann, & Unser, 1998), Lucas-Kanade framework

based algorithm (Greenberg & Kerr, 2009) and etc. Motion correction step guarantees that the average fluorescence intensity recorded over time belongs to the selected region of interest (ROI) and not to the neighboring areas due to the shift in XYZ space.

Advanced mathematical algorithms have been introduced to deal with the automatic ROI selection in a high dimensional spatiotemporal Ca^{2+} imaging data. In particular, some of these algorithms focus on activity-dependent ROI segmentation (Eran A. Mukamel, 2009; Junek, Chen, Alevra, & Schild, 2009; Miri, Daie, Burdine, Aksay, & Tank, 2010; Ozden, Lee, Sullivan, & Wang, 2008). First, they use an efficient dimension reduction algorithm like principal component analysis (PCA) to reduce the dimensionality and noise level in the dataset. This step then is followed by source extraction techniques such as Independent Component Analysis (ICA) (Eran A. Mukamel, 2009), Nonnegative Matrix Factorization (NMF) (Pnevmatikakis et al., 2016), clustering-based methods (Pachitariu et al., 2016) or dictionary learning (A. Petersen, Simon, & Witten, 2017) to extract ROIs automatically. These algorithms unsupervisedly analyze temporal information jointly with corresponding spatial location of active neurons.

Unsupervised algorithms show an advantage over supervised algorithms in a large-scale recording when spatial resolution is low, and fluorescence intensity of populations of neurons is encoded in a single pixel. In this situation, a priori information about ROI's location is not available, and the algorithm cannot rely on this information. In the case of high spatial resolution, extracted temporal data for each neuron allow inferring spike train using deconvolution techniques (Vogelstein et al., 2010). Additionally, supervised algorithms (Sasaki, Takahashi, Matsuki, & Ikegaya, 2008; Theis et al., 2016) can estimate accurate spike trains from Ca^{2+} transients in the cost of labeled data. For labeled data acquisition, simultaneous

Ca^{2+} imaging and electrophysiological recordings of the same cell are needed. However, this type of recording could be costly or in some cases, not possible. For a detailed comparison between techniques see (Berens et al., 2018).

Beside analyzing temporal traces belonging to individual neuron, functional dependency among spatially distinct neurons in ensemble population or, at larger scale, among multiple brain regions reveals functional connectivity patterns in a given circuit. In general, the functional connectivity among various samples can be described using model-free methods such as descriptive statistical methods (Cohen & Kohn, 2011; Fujisawa, Amarasingham, Harrison, & Buzsáki, 2008; Sutera et al., 2014), information theory based techniques (Garofalo, Nieus, Massobrio, & Martinoia, 2009; Orlandi, Stetter, Soriano, Geisel, & Battaglia, 2014; Schreiber, 2000), supervised learning-based algorithms (Veeriah, Durvasula, & Qi, 2015) or model-based methods like Dynamic Bayesian network (DBN) (Eldawlatly, 2013), maximum entropy model (Tkacik et al., 2014) or generalized linear model (Song, 2013). The features describing neuronal connectivities are the existence of connection, cause of interaction, significance, and dynamic of the network. The major challenge in model-based connectivity is the problem of overfitting or underfitting. The solution suggested for this problem is mainly to infer the connectivity jointly with regularizer on cost function (constrained optimization).

Aim of the project

As explained above, the early development of the brain is driven by highly intricate and hierarchic patterns of the endogenous activity. Intrinsic (spontaneous) activity patterns have been seen, in vivo and in vitro, in many brain regions. However, these studies focused on these specific brain regions only and therefore large-scale endogenous activity patterns that orchestrate the brain development, as well as connectivity map including different brain regions is not well understood.

In this work, we developed an analyses pipeline by applying the state-of-art mathematical algorithm for analyzing large-scale neuronal activity in the cortex of neonatal mice. By taking advantage of fast and large-scale in vivo imaging, the aim was to (i) characterize the patterns of large-scale neuronal activity in the dorsal cortex of neonates, (ii) identify the areas with correlated activity patterns and (iii) establish the relationship between anatomical- and activity-driven cortical maps.

Materials and Methods

Mice

All experiments were conducted in accordance with institutional animal welfare guidelines and were approved by the state government of Baden-Württemberg, Germany. For consistency, we focused on a defined animal age (P3) because during the first postnatal week the rapidly developing rodent cortex is known to traverse several developmental states (Kirischuk et al., 2017).

In line with the biometric planning, seven 3-day-old nestin-Cre x Ai95(RCL-GCaMP6f)-D mouse pups of either sex were used in this study. Parent mouse lines B6.Cg-Tg(Nes-cre)1Kln/J and B6;129S-Gt(ROSA)26Sortm95.1(CAG-GCaMP6f)Hze/J were originally obtained from Jackson Laboratory (stock № 003771 and stock № 024105, respectively) and were bred on the C57BL/6 background. Note that in the widely used B6.Cg-Tg(Nes-cre)1Kln/J mouse strain (https://www.jax.org/ strain/003771) expression of the Cre recombinase becomes widespread only during the perinatal development (around P0; (Liang, Hippenmeyer, & Ghashghaei, 2012)). This late expression of both the recombinase and the Ca^{2+} sensor in our experimental mice minimizes the risk for any unwanted side effects, including the eventual toxicity or the development of aberrant activity (compare our Figure 14A to Figure 3 and 6 in ref. (Steinmetz et al., 2017)).

Animal preparation for *in vivo* Ca^{2+} imaging

Mouse pups were anesthetized with isoflurane (2.5% for induction, 1-2% for the rest of surgery). The skin above the dorsal part of the skull was cut away, the connective tissue was gently peeled off, and the custom made ring-like plastic chamber was glued to the skull. Xylocaine gel (2%) was applied to the wounded skin edges. To

prevent the skull from drying out, it was covered with agarose (1-2%) dissolved in standard Ringer's solution containing (in mM): NaCl 125, KCl 4.5, $MgCl_2$ 1, $CaCl_2$ 2, $NaHCO_3$ 26, NaH_2PO_4 1.25, Glucose 20, pH 7.4. The procedure described above lasted 23 ± 3.8 min (n=7 mice). After that, the isoflurane anesthesia was terminated, and the animal was allowed to recover on a warming plate (34^{o}C - 36^{o}C) for at least one hour.

In vivo large-scale single-photon Ca^{2+} imaging

After recovery the animal, resting on a warming plate, was transferred into the imaging setup and head-fixed under the MVX10 Research Macro Zoom Microscope equipped with an LED source for excitation (Thorlabs, central wavelength 470 nm), the Zyla 4.2 sCMOS camera (Andor Technology) and Andor Solis software for image acquisition. Animal's limbs were free to interact with each other and the surface of the warming plate (schematic is illustrated in Figure 3). Both the left and the right hemispheres were imaged simultaneously through the intact skull at 256x256 pixel resolution (1 pixel ≈ 50x50 μm^2) and 11 ms/frame for half an hour (three consecutive 10-min-long acquisition series). Although the nestin promotor driving the Cre recombinase activity in our mice is expressed in both neuronal and glial cell precursors and the imaging technique used does not differentiate between neuronal and glial signals, following data suggest that the signals analyzed in the current study are of neuronal origin: (i) between P0 and P3 neurons represent ~ 88% of all cells in the rodent cortex (Bandeira, Lent, & Herculano-Houzel, 2009) (ii) kinetic properties of population Ca^{2+} signals in these preparations coincide with those of neuronal Ca^{2+} transients and differ significantly (approximately by order of

magnitude) from those of glial Ca^{2+} transients (Adelsberger et al., 2005; Golshani et al., 2009).

Recordings of animal's movement

Animals were imaged with a monochrome infrared (IR) light-sensitive camera. IR LED (950 nm) was used for illumination. To remove the salt-and-pepper noise, the image sequence (720x480 pixels, 29 Hz) was filtered with a median filter of kernel size 3x3.

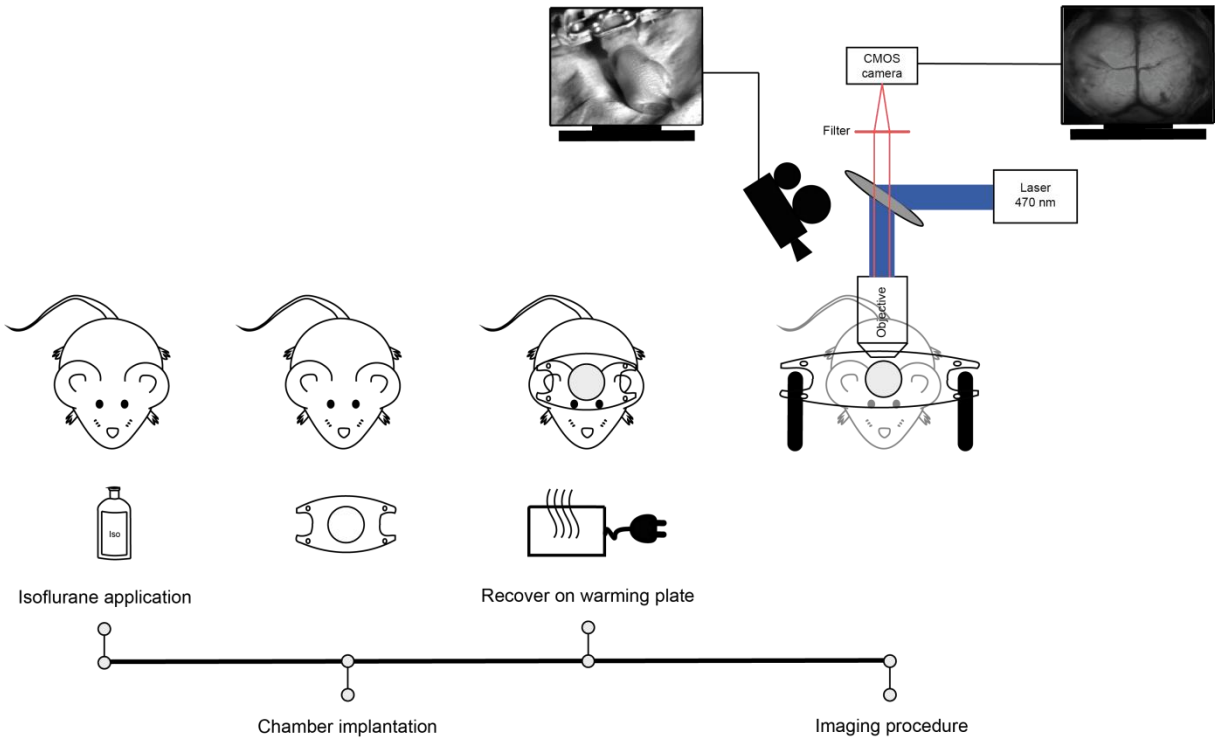

Figure 3. The schematics of the experimental procedure. Left panel provides a schematic view to isoflurane application at the beginning of the experiment. The second panel indicates the chamber implantation step to fix the head during recording. The third panel shows the recovery procedure on the warming plate. The last panel illustrates the recording procedure using a head-fixed mouse. It consists of three schematic diagrams that briefly shows the recording procedure: (i) head-fixed mouse under microscope, (ii) infrared (IR) light-sensitive camera and its recording software in the left corner that records the body motion of the animal parallel with Ca^{2+} imaging and (iii) simplified schematic diagram showing principle of light microscopy used in this experiment.

Subsequently, adjacent frames were pixel-wise subtracted from each other, thus transforming the original image sequence into an image sequence containing the information about the temporal changes within the field of view (Lipton, Fujiyoshi, &

Patil, 1998). For a given resulting image, the sum of absolute values of all pixels was taken as a measure of instantaneous body motion. Subsequently, the movement trace was upsampled using Matlab's 1D interpolation function to match the sampling rate of the Ca^{2+} signals (~91 Hz), plotted over time, normalized to the maximum recorded value, thresholded at ~6% to eliminate breathing artifacts and used to create a binary signal where all ones corresponded to the motion period and all zeros corresponded to the resting state (Figure 9). The on/off switching of the 470 nm excitation light, seen by both cameras, was used to synchronize the imaging of Ca^{2+} and movement signals. Also, we defined the time window including one second before the movement onset and three seconds after the end of the movement (corresponding to the decay time of the eventual movement-evoked Ca^{2+} signals) as a transition state. With this procedure, the behavior of the animal was automatically subdivided into three different states: motion, rest, and transition (see Figure 10).

As the motion state potentially contained either spontaneous muscle twitches (Blumberg, 2010) or generalized movements, in a separate series of experiments we recorded nuchal muscle electromyogram (EMG (Seelke, Karlsson, Gall, & Blumberg, 2005)) simultaneously with imaging body movements. Note that at P3, the EEG traces are discontinuous, thus providing no information about the vigilance states (N., B., J.L., R., & M., 2018). For EMG recordings a stainless steel wire (type SS-3T, Science Products GmbH, Hofheim, Germany) was used. Two to five mm of the insulation was stripped off, and the insulation-free ends of the wire were gently inserted subcutaneously and placed bilaterally on the top of the neck muscles.

After the correct position of the wires has been verified, the wires were fixed to the ring-like plastic chamber (see above) with a UV-cured dental cement. EMG data

were recorded at 1 kHz (0.3-500 Hz band-pass filter) using the Powerlab differential amplifier (ADInstruments Ltd, Oxford, United Kingdom).

Movement binary signal was created from the EMG signal using signal envelope analysis (Oppenheim & Schafer, 2009). The normalized cross-correlation between the movement signals extracted from the imaging and the EMG data showed peak values of 0.6-0.85 (n = 9 recording in 3 mice) suggesting that both signals faithfully reflect the structure of the animal's movement. Note, however, that some tiny movements, as well as limb twitches, might remain unrecognized by either one or even both techniques (Seelke et al., 2005). Next, we separately used EMG- and imaging-based data sets of individual animals to construct the distributions of the duration of movement episodes. Both data sets identified the first peak at 350-600 ms, followed by a local minimum at 700-800 ms. Based on this data, we chose 750 ms as an empirical border between spontaneous muscle twitches and generalized movements. For mice included in the present study, muscle twitches represented 39.5 ± 14 % of all movement events (n=6 mice) and the fraction of time covered by muscle twitches ranged between 5% and 16% (median per mouse) of the total movement time. We concluded, therefore, that under our experimental conditions, Ca^{2+} signals recorded during the animal's movement mainly reflect the ones associated with generalized movements.

Data analysis

Recording high-speed large-scale images throw intact skull is an advanced technique helping to understand neuronal activities and their interactions on a meso- and macroscales. However, it produces data in the range of ~40GB/h (taking spatial resolution of 256 x 256 pixels and the acquisition speed of 91 frames/sec). Storage and processing of this amount of data is a challenging task. To solve this

task one needs robust, automatic, fast, and scalable to large data sets computational tools. Here, we developed a reach analyses pipeline that helps to process large-scale Ca^{2+} fluorescence data. This pipeline contains four main branches (Figure 4B) analyzing the recorded data in a spatiotemporal manner. First two branches, in two different algorithms, calculate the pattern of activity. The third branch considers temporal dependencies within spatial patterns, and the last branch calculates functional connectivity among multiple cortical regions. All branches receive their inputs after motion correction step where the data frames are corrected for motion artifacts based on a given template frame. Below, we explain the whole pipeline in detail.

If not otherwise indicated, data analyses started with reducing the image size to 128x128 pixels using 2x2 binning.

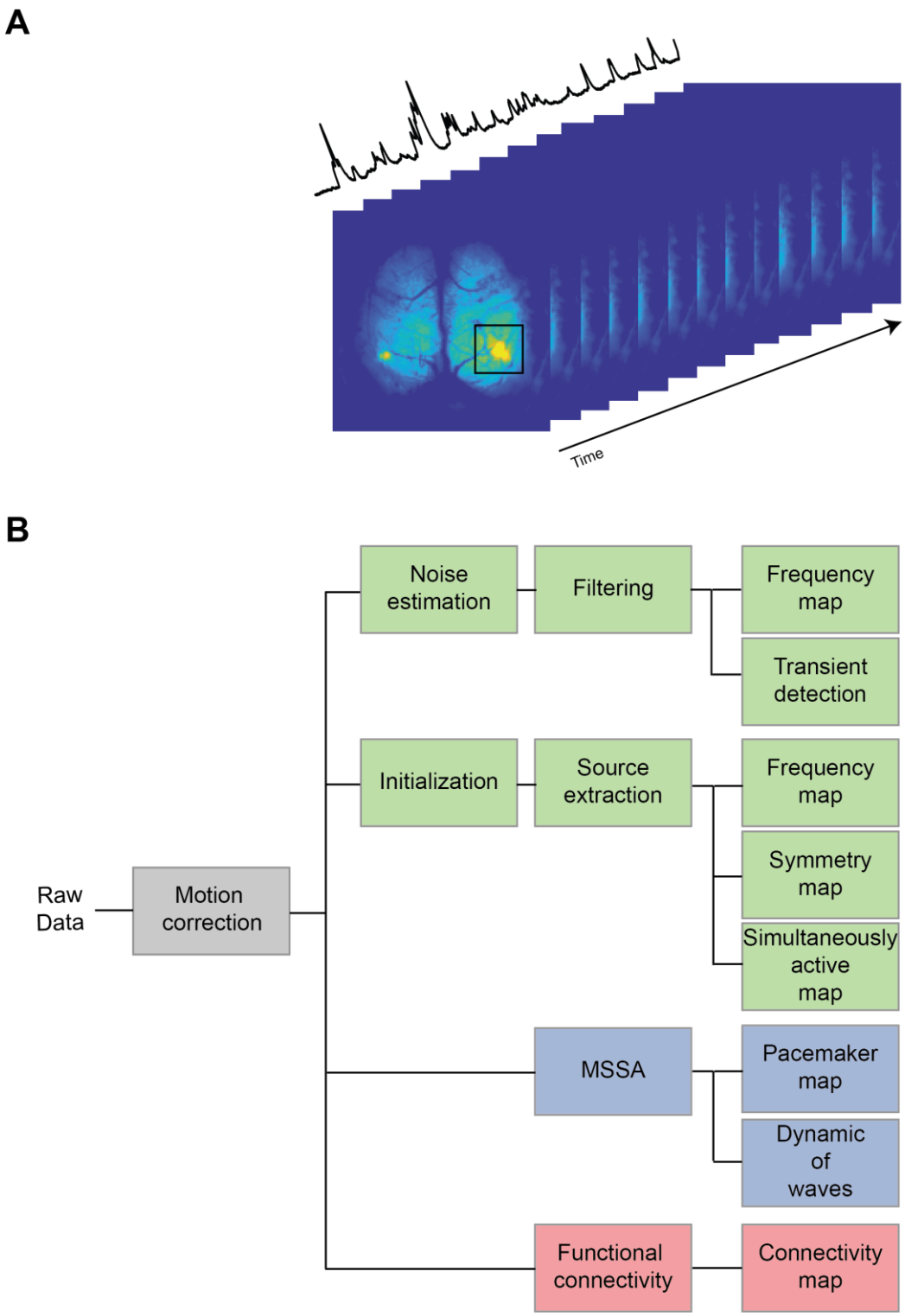

Figure 4. Analyses pipeline. (A) Representative fluorescence intensity frames recorded from neonatal P3 mouse cortex. Black arrow indicates time axis. The black box shows typical local cortical activity, and its average fluorescence intensity expanded parallel to the time axis (black trace). (B) Diagram illustrates our analyses pipeline. This pipeline starts with the motion correction step, and its output is taken as a common input into all branches. The diagram contains four main branches that output three main results. These three outcomes are categorized based on three different colors. Light green represents branches that analyze spatial activity patterns. Light purple shows the branch that focuses on temporal dependencies within spatial patterns and light red branch calculates functional connectivity.

Motion correction

Intensity-based image registration algorithm was used to remove motion artifacts in each video (Figure 5). This process is an automatic and iterative approach to do motion correction task. It takes a pair of images, a metric, an optimizer, and a transformation type. Similarity or dissimilarity between two images as a quantity is given by the metric. This value then evaluates the accuracy of misalignment correction. The optimizer is a method to minimize the dissimilarity or maximize the similarity, and the transformation type is a strategy that aligns the misaligned image with the reference image. The process starts with defining the transformation type. Then using this, the misaligned image is bilinearly interpolated. Next, the metric computes the value of similarity between the transformed misaligned image and the reference image. This value is compared to stop criteria and defines the process termination or continuation. In the case of continuation, the optimizer calculates new transformation, and the cycle will be repeated. The stop criteria mainly depend on two parameters, the maximum number of iteration and metric value.

To do motion correction, we used Matlab image processing toolbox and custom-written code.

Pixel-wise detection and analyses of Ca^{2+} signals

In our analyses pipeline, the first branch focuses on the information provided by each pixel in the given video. This analysis channel contains noise-estimation, filtering, transient detection and pixel-based frequency map creation steps. In this analysis line, temporal information from each pixel is taken and processed, results are returned to the spatial location of the selected pixel. Below we describe each step in detail.

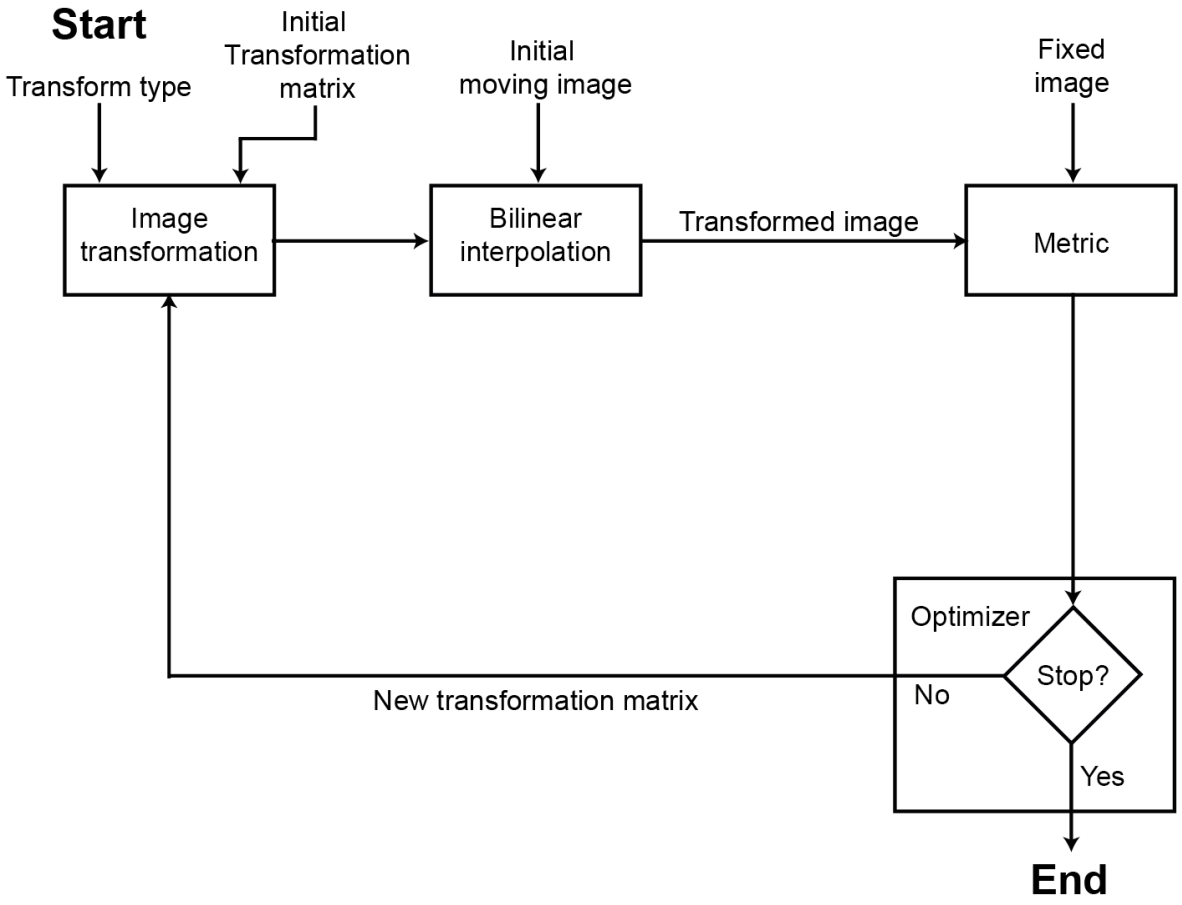

Figure 5. Block diagram of the image registration process. This analysis cycle shows the iterative approach in motion correction algorithm. The cycle in each iteration starts with defining the transformation type. In the first iteration, the initial transformation matrix has to be provided. The second block shows bilinear interpolation of the misaligned image using information from the previous step. The third block represents a computational procedure that calculates similarity or dissimilarity between reference and misaligned images. The last block as an optimizer defines the method to minimize the dissimilarity or maximize the similarity. This process stops if the stop criteria are reached.
This diagram is taken from the MathWorks website (www.mathworks.com/help/images/intensity-based-automatic-image-registration.html).

Noise estimation

The noise in a given data was estimated using Principal Component Analysis (PCA) algorithm as follows: after decomposing data to linearly uncorrelated variables named principal components (Figure 6B), the sorted components were split into two parts, depending on their eigenvalues (Figure 6C). To use data in the original space, two videos based on split components were reconstructed.

A threshold was chosen such, that the components from the first part described 95% of data variance. This selection guarantees that the reconstructed video contains all information. The video reconstructed with the first part of the components were interpreted as data, and the video reconstructed with the rest of the components were interpreted as noise (Figure 6D).

Filtering

Next, to remove contamination of any non-transient slow oscillation from each signal (fluorescence intensity of each pixel in time), high-pass filter at the cut-off frequency of 0.05 Hz was designed and applied to the traces of each pixel in the reconstructed data. Zero-phase filtering strategy was used to avoid any time shift between wave shapes of the filtered signal and the original signal (Figure 6E). The example of the original and filtered traces is shown in Figure 6F.

Transient detection

Following the analysis line, in the data taken from the previous step, the fluorescence changes in each pixel of the video with peak amplitudes larger than the fourfold of the SD, in each corresponding pixel of the reconstructed data containing noise, of the baseline noise were detected using the Matlab (MathWorks) peak detection function. Based on the known kinetics of GCaMP6f (Chen et al., 2013), we eliminated the events with the full width at half maximum (FWHM) of less than 100 ms. The rest of the detected events were defined as Ca^{2+} signals and were used for further detailed analyses.

Pixel-based frequency map

The numbers per minute of the detected Ca^{2+} signals were used to create the color-coded frequency maps. These numbers, calculated separately for each pixel, were located on spatial coordinates of corresponding pixels. These maps were created separately for three different behavioral states (motion, rest, and transition). The temporal location of each peak determines that it belongs to each behavioral state. The binary motion signal, explained above, was used to define the time window of each behavioral state.

Model-based detection and analyses of Ca^{2+} signals

Detecting active regions automatically in the wide-field image is a challenging task. A proper algorithm is necessary to extract the activity sources in a meaningful and unsupervised way. Moreover, it has to extract temporal information jointly with a spatial location of activities in a given spatiotemporal dataset. Non-negative Matrix Factorization (NMF) is a model that unsupervisedly extracts the sources and provides both temporal and spatial results.

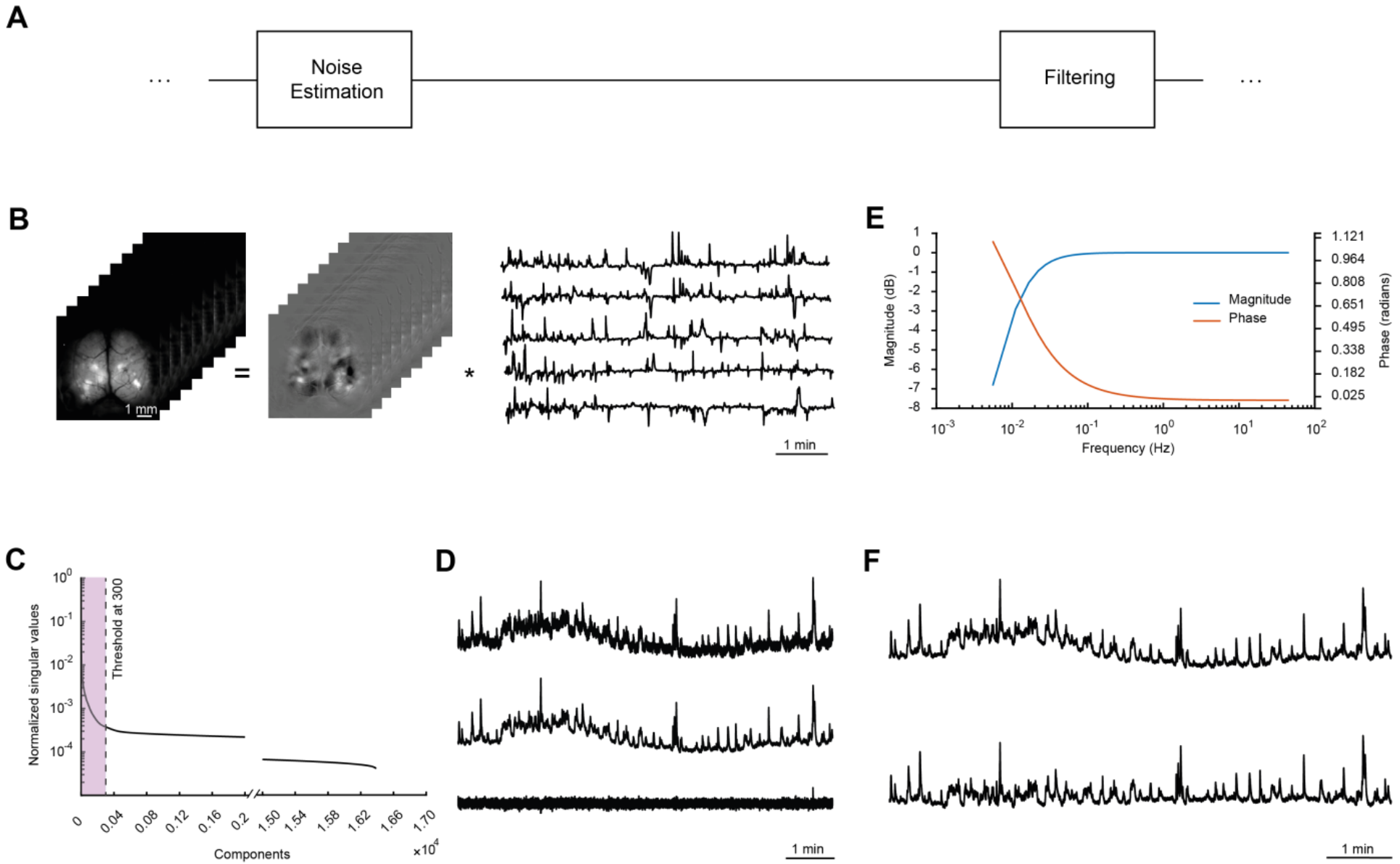
A
Noise Estimation
Filtering
B
1 mm
=
*
1 min
C
Normalized singular values
Threshold at 300
Components
×10^4
D
1 min
E
Magnitude (dB)
Phase (radians)
Magnitude
Phase
Frequency (Hz)
F
1 min

Figure 6. Analyses of pixel information. (A) Block diagram of the analyses procedure. (B) Illustrates the PCA transformation on the original video. The right side of the equal sign are the principal components, and transformed data where their multiplication results in the original video. (C) This panel represents normalized singular values in the log-scaled graph. The x-axis has been shortened between 2000 and 15000. (D) Representative noise-reduced fluorescence trace. First trace (up) is an unprocessed representative data. Middle trace is noise-reduced version of the upper trace, and the lower trace is an estimated noise. (E) Bode plot of high-pass filter used to remove slow oscillations. Magnitude and phase of bode plot have been shown in blue and red colors respectively. (F) Same trace as in D (middle trace) filtered using a high-pass filter with characteristic indicated in E. Upper trace (middle trace in D) is an unfiltered data and lower traces is high-passed filtered data at the cut-off frequency of 0.05 Hz.

Region of interest detection based on source extraction

Pixels that showed a coherent change in fluorescence intensity were grouped into ROIs using NMF algorithm, running on a full data set. According to NMF, a given data matrix X is factorized into two matrices W and H containing spatial filters (W) and the corresponding time information (H): X= WH (an example is illustrated in Figure 7), $W_{ik} > 0$ & $H_{kj} > 0$. W and H can be calculated by minimizing the cost function, $min_{W,H}\|X - WH\|_F$. In case of the low-rank NMF, the rank (k) of W and H is set to be smaller than the dimension of X. As an optimizer to minimize the cost function, we have chosen the alternating least-squares algorithm (Berry, Browne, Langville, Pauca, & Plemmons, 2007). The initialization method was based on Independent Component Analysis (ICA). The rank of W and H was estimated by PCA component's coefficients.

Simplified ALS algorithm for NMF calculation

***W_0** = Initialize*

for iteration = 1: maxiter

*Least square step, Solve optimization for **H**: **$W^TWH = W^TX$***

*Nonnegative constraints, Project all negative values in **H** to 0*

*Least square step, Solve optimization for **W** while **H** is kept fix: **$HH^TW^T = HX^T$***

*Nonnegative constraints, Project all negative values in **H** to 0*

end

The 300 spatial filters were inspected by eye. Filters resembling either the blood vessel pattern or whole-brain image contaminated by blood vessel pattern, likely reflecting movement artifacts, were discarded. The total number of such filters was in the range of 45-120. The remaining filters contained groups of bright neighboring pixels, clearly discernible from the noisy background. Sobel edge detector algorithm (Lim, 1989) was used to define the border between the active and background pixels. The frame-wise noise was estimated using these background pixels. Finally, the filters were binarized using the threshold value of fourfold the SD of the corresponding background noise. Groups of connected pixels with n > 10 pixels were defined as ROIs. The filters containing one ROI were called **single ROI filters,** and the ones with more than one ROI were called **multi-ROI filters**.

ROI-based frequency maps

To create ROI-based frequency map, each ROI was weighted by ascribing a value equal to a number of peaks detected in its temporal domain (H). For peak detection, traces corresponding to spatial filters (W) were thresholded at 95% of their maximal amplitude. Finally, the weighted ROIs were superimposed to create a color-coded ROI-based frequency map. These maps were created separately for two different behavioral states (motion, rest). Same as above, the temporal location of each peak determines that it belongs to which behavioral state.

Symmetry maps

For calculation of the cortical symmetry maps, first, the brain rotationally corrected according to mid-line between two hemispheres. Then, one hemisphere was mirrored to another against the mid-sagittal plane and all ROIs belonging to each

multi-ROI filter were examined pairwisely by calculating their two-dimensional correlation coefficients. A pair of ROIs was considered as symmetric if the correlation coefficient was ≥0.5. Filters which contained only symmetric ROIs were classified as **total symmetry filters,** and filters with at least one pair of symmetric ROIs were classified as **semi-symmetry filters**. Further, according to their corresponding time information (matrix H) and the animal state, the symmetry filters were subdivided into two categories: motion and rest. Superpositions of filters of a given class and category were used to produce specific symmetry maps.

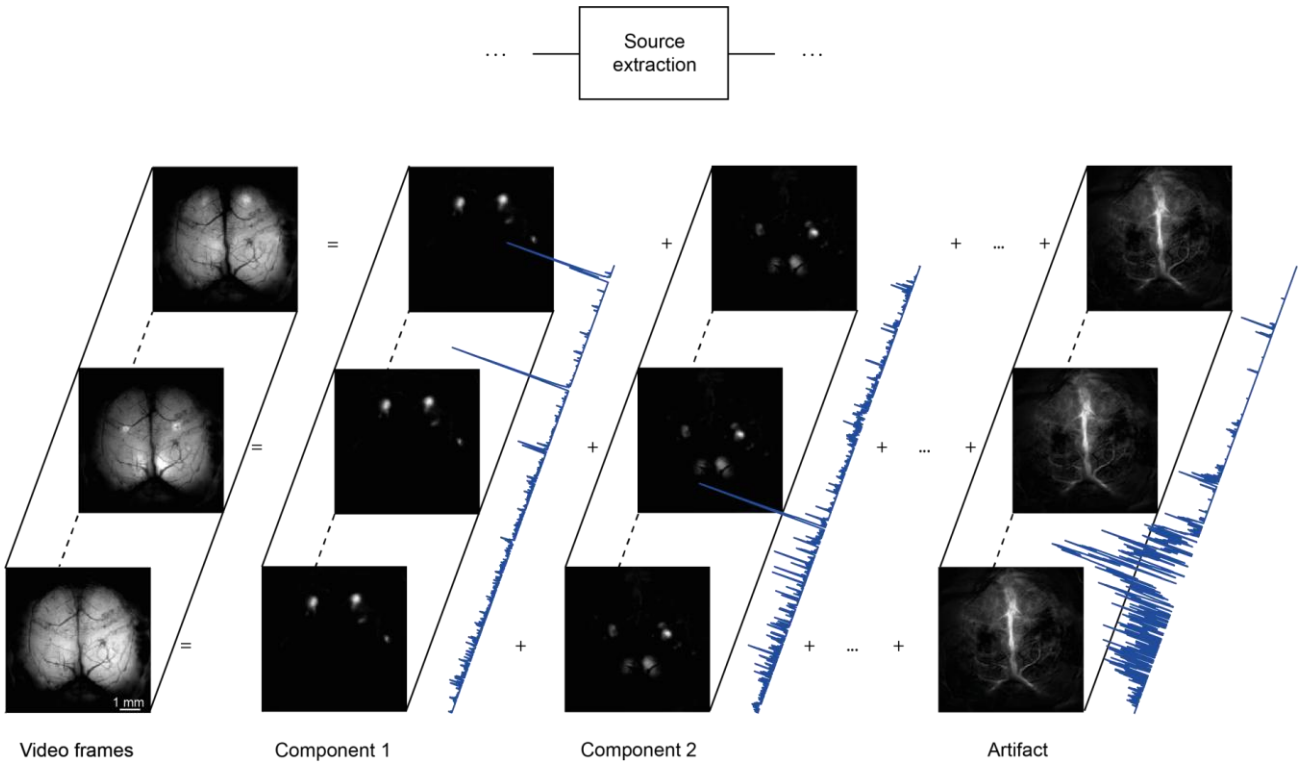

Figure 7. NMF based source extraction. This figure illustrates source extraction from a given video using NMF algorithm. The first column shows frames of the video aligned in the time axis. The other three columns are examples of the extracted sources (components) with their sums reconstructing the original video. Temporal information related to each source is plotted parallel to the time axis in blue (for more detail please see Methods).

Map of simultaneously active cortical regions

To identify brain regions synchronously active during the movement and the resting states, spatial filters in multi-ROIs obtained from NMF analysis (see above) were processed according to the time information (matrix *H*) and the animal state. Then, the subregions from each multi-ROI were assigned to the anatomical regions based on the location of their center of mass. For any multi-ROI filter, each pair of simultaneously active subregions (within each cortical region or between two distinct cortical regions) was represented by an entry in the matrix (10x10 - each row or column) corresponds to one of the cortical regions. Such entry was made each time when the two subregions were simultaneously active. This procedure was repeated for all multi-ROIs in motion and resting states providing two matrices. Then each matrix was normalized to the sum of both matrices and values below 50% were removed, to focus on interactions, predominant for each state. Median of three matrices (three 10-min-long image series) was taken as a representative map for each mouse and median of all maps from n = 6 mice was depicted as a summary result.

Wave analyses

Data revealed that the cortical activities are organized into the patterns that are shaped in both space and time. One approach to investigate temporal dynamics of Ca^{2+} waves jointly with their spatial location is to consider dataset as a multichannel time series. These time series contain multiple unknown temporal patterns with different spectral structures, noise, and non-stationary elements. Thus, the model-free technique is required to decompose the multi-channel time series into a mixture

of interpretable components. Performing Multi-channel Singular Spectrum Analysis (MSSA) results in model-free decomposed spectrums.

Multi-channel Singular Spectrum Analysis (MSSA)

To detect propagating Ca^{2+} waves, the image sequences were processed by the nonparametric spectral estimation method: Multi-channel Singular Spectrum Analysis (MSSA; (Olshevsky, Tyrtyshnikov, Golyandina, & Usevich, 2010)). Before being reshaped into a two-dimensional space, the data were down-sampled by a factor of 10 in the temporal domain and by 25 in spatial domain.

The basic algorithm of MSSA

first, centralize the data $D_{n\times p}$ by subtracting the mean value of each pixel

$D_{n\times p} = \begin{bmatrix} x_{11} & \cdots & x_{p1} \\ \vdots & \ddots & \vdots \\ x_{1n} & \cdots & x_{pn} \end{bmatrix}$*, n is the number of samples, p is the number of the pixels in the images*

then calculate the embedding matrix M,

$M_{N^{'}\times pk} = \begin{bmatrix} x_{11} & x_{12} & \cdots & x_{21} & x_{22} & \ldots \\ x_{12} & x_{13} & & x_{22} & x_{23} & \ldots \\ \vdots & & \ddots & \vdots & & \\ x_{1n-1} & x_{1n} & \cdots & x_{2n-1} & x_{2n} & \ldots \\ x_{1n} & 0 & & x_{2n} & 0 & \ldots \end{bmatrix}$*,* $N^{'} = n - k + 1$ *and K is a lag shift (this matrix called Hankel matrix)*

using embedding matrix M, estimate covariance matrix C, $C_{pk\times pk} = \frac{1}{N^{'}} M^{'} M$

Calculate eigen decomposition of covariance matrix,

[eigen value, eigen vector] = eigen decomposition (C).

Reconstructing time series

$X = \sum_j X^j$, where X is the original dataset and X^j is reconstructed data based on each or group of components.

Then, $M = \sum_j M^j$, where M^j is the embedding matrix from each component.

Each M^j can be reconstructed using eigen vector and projected data.

if M^j has Hankel structure,

> *values of reconstructed X^j are the averages of the corresponding anti-diagonals of the matrix M^j*

elseif M^j has NOT Hankel structure,

> *first M^j has to transformed to Hankel matrix*
> *then, X^j can be reconstructed as above*

end

In the MSSA, each principle vector describes an oscillatory component in the data set, whereas principle components represent the corresponding weighting coefficients. The k value (lag shift) was set to 15 s.

Pacemaker maps

Data were reconstructed (MSSA (Olshevsky et al., 2010)) based on a subgroup of components (sorted components 20-150). The remaining components represented either noise or slow baseline drifts. Finally, the reconstructed data were spatially thresholded to obtain the corresponding binary mask of each frame. Thresholding was based on fitting Laplace distribution to the reconstructed data. As a threshold, we selected a fourfold of the scale parameter of the estimated Laplace distribution. The first frame of each wave was defined as its pacemaker region.

Dynamic of waves

Populations of connected pixels were treated as objects and dynamics of each object in time represented a single wave. The distance traveled by each wave was characterized by the displacement of the corresponding object's center of mass. The waves were divided into two groups: (1) stationary waves with the center of mass moving less than 200 µm and (2) propagating waves with the center of mass moving more than 200 µm. Further, we counted the waves propagating within a given cortical region and calculated the fraction of waves occurring during the motion and resting periods, respectively. A similar procedure was applied to calculate the fraction of waves propagating between any two cortical regions.

Functional connectivity

The large-scale cortical recordings give the possibility to observe all cortical regions simultaneously. Consequently, this facilitates the investigation of any local cortical activity in the context of surrounding cortical regions. Also, tracking short- and/or long-range coherent activities determines the functional properties of neuronal networks (Friston, 2011). Taking all, studying the functional connectivity by means of Ca^{2+} imaging reveals local networks as well as long-range cortical functional connections. However, studying cortical functional connectivity could be biased by deep unobserved activity sources. Therefore it is better to go for analyses of direct connectivity (S. M. Smith, 2012; S. M. Smith et al., 2011).

For calculating direct connectivity maps, input data were binned five by 5 pixels, temporally down-sampled by a factor of 10 and centered in the time domain by subtracting the mean value of each pixel. After that, the connectivity maps were calculated separately for resting and motion periods by using the sparse partial

covariance algorithm (Ma, Xue, & Zou, 2012). Assuming that data are drawn from a multivariate Gaussian distribution, elements of the precision matrix $\sum^{-1}$ explain partial covariance in a given data set. Sparsity constraint was introduced by adding an extra penalty term to the likelihood function. To calculate the sparse partial covariance one has to maximize the penalized log-likelihood L (Friedman, Hastie, & Tibshirani, 2008),

$$argmax_{\theta} L = log\ det(\theta) - tr(S\theta) - \gamma \|\theta\|_1$$

where $\theta = \sum^{-1}$, and S is an empirical covariance matrix

$\| \|_1$, is l_1 norm and γ is sparseness tuning parameter.

The sparse partial covariance was calculated with a range of different γ values. The smaller γ values provide more dense connectivity pattern, whereas the larger γ values increase sparseness in the connectivity map by removing weak connections between the nodes. We identified the values 1.4 and 1.8 as cornerstone values supporting in one case a consistent and recognizable dense connectivity pattern and in another case a sparse stable pattern that was independent of a small variation of γ value.

Connectivity maps

After obtaining the direct connectivity map, pixels belonging to specific cortical regions were identified using the corresponding anatomical map of the brain (like the one shown in Figure 9A). Partial covariances between pixels of each specific cortical region were summed up, giving the value α_{ij}, where α_{ij} reflects the strength of the connectivity within the given cortical region if i=j. Similarly, partial covariances between pixels belonging to a pair of specific cortical regions were summed up, contributing those values of α_{ij} (i≠j), where α_{ij} reflects the strength of the connectivity

between the two different cortical regions. Finally, all values were normalized to the maximal α_{ij} value.

Statistical analyses

Statistics were performed using JASP and SPSS software. Normality of data was tested using the Shapiro-Wilk test. The two-tailed paired Student's t-test was used for pair-wise comparisons of normally distributed data sets. For pair-wise comparisons of not normally distributed data, the Wilcoxon signed-rank test was applied. One-way or two-way repeated measures ANOVA (rANOVA) was used for comparing more than two normally distributed dependent variables. In the case of not normally distributed data, the Friedman test was used. In rANOVA sphericity assumption was tested using Mauchly's test, and in case of sphericity violation, Greenhouse-Geisser correction was applied. All ANOVAs, which show significant results, were followed by a post-hoc test with Hold-Sidak correction for multiple comparisons. For all tests, differences were considered significant if $P < 0.05$.

If not otherwise indicated, data are presented as the median ± interquartile range (IQR)).

Results

Patterns of the large-scale cortical activity in the neonatal cortex

When imaging through an intact skull (Figure 8A-C), we observed two kinds of cortical activity in the dorsal mouse cortex: local Ca^{2+} signals, involving one or several anatomical regions (Figure 8B, upper panel) and global Ca^{2+} signals. Placing regions of interest onto major anatomical regions of the dorsal cortex (i.e., visual, auditory, somatosensory and motor cortices) revealed that global Ca^{2+} signals often invaded all anatomical regions (Figure 8C), whereas the local did not. Taking the fact that the cortex of neonates mouse in P3 is not functionally mature, when selecting anatomical regions (Figure 8A) we relied on the atlas-based knowledge (Allen Institute for Brain Science, 2015) combined with data provided by (Gee et al., 2014). Simultaneous recording of animal movements (consisting at this age of muscle twitches and generalized movements, see Methods for details about the estimation of movement's nature) by means of an infrared imaging camera (gray trace in Figure 8C; Figure 9), revealed the presence of spontaneous Ca^{2+} signals during both moving and resting states. Temporal relations, as well as signal strength between Ca^{2+} and motion signals as a representative case, are illustrated in figure 9.

Behavior discrimination of animal

Recording body movement using infrared camera revealed that the animal behavior could be split into two states: resting state when there is no detectable movement observed and motion state. To clearly discriminate between the motion and the

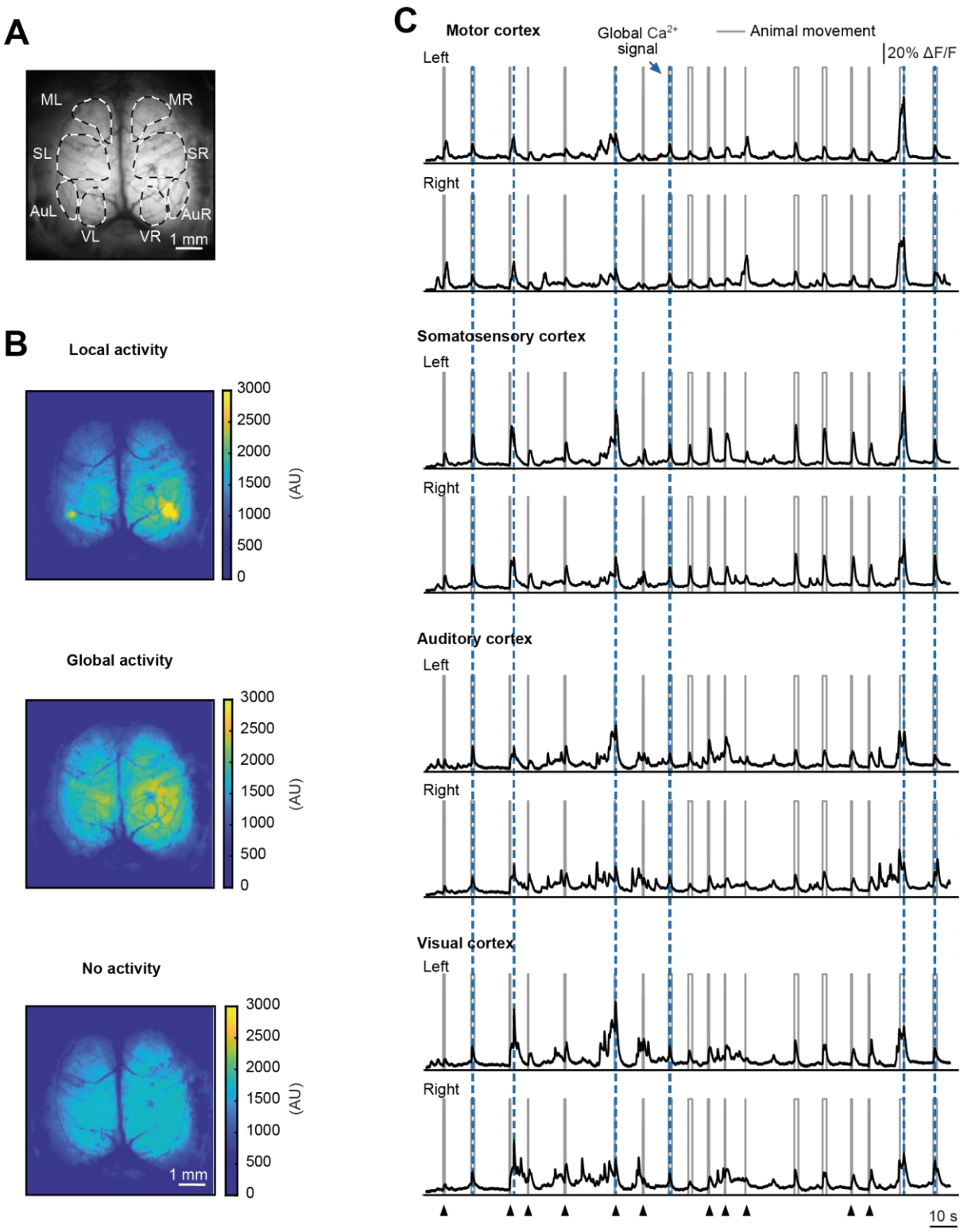

Figure 8. Large-scale cortical activity in the neonatal mouse cortex. (A) Top view on a P3 mouse cortex taken through an intact skull. Broken lines delineate cortical regions of interest (estimated as in (Gee et al., 2014)): ML, MR - motor cortex (left and right), SL, SR - somatosensory cortex (left and right), AuL, AuR - auditory cortex (left and right) and VL, VR - visual cortex (left and right). (B) Averages of 100 consecutive autofluorescence-subtracted images taken during periods of either local (top) or global (middle) cortical activities or no activity (bottom). Autofluorescence values are averages of data recorded in two different 3-day-old C57BL/6 mice, subtraction was done for display purposes only. Image brightness (arbitrary units, AU) is color-coded, with warm colors reflecting higher values. (C) 200-second-long ΔF/F traces recorded from ROIs delineated in A. Gray boxes mark time periods of animal's movement and blue dashed lines indicate the time periods during which global (i.e., detected simultaneously in >70% of all recorded cortical pixels, see arrow on the top graph) Ca^{2+} signals were recorded. Arrowheads mark muscle twitches.

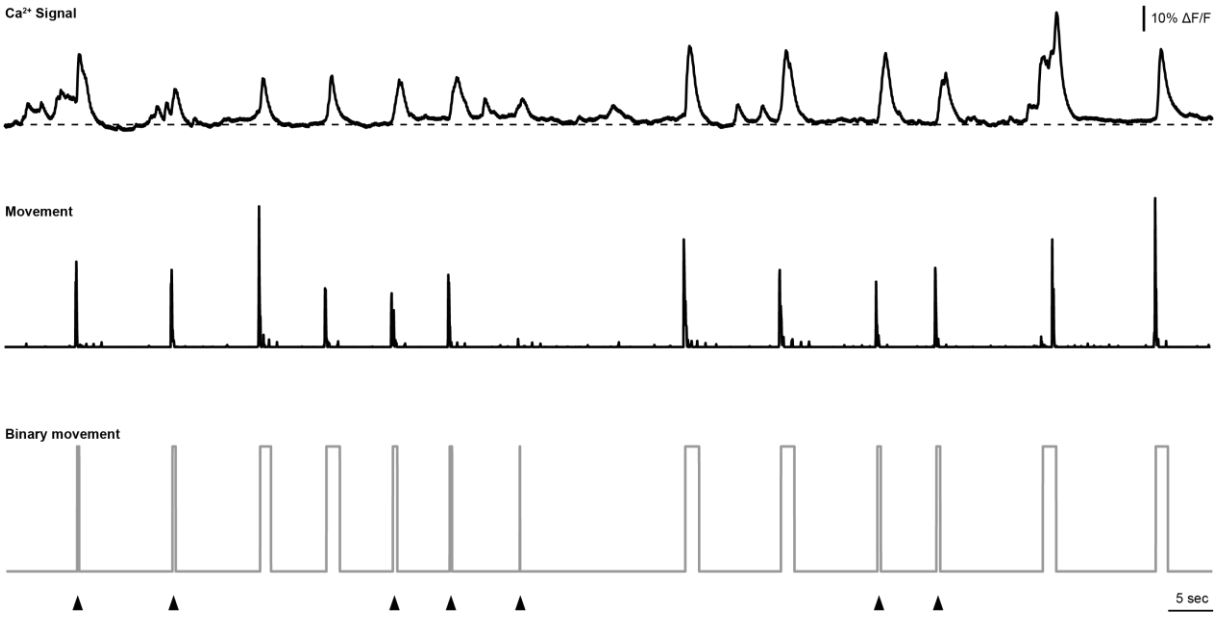

Figure 9. Signal strength between Ca^{2+} and motion signals. Example traces illustrating Ca^{2+} signals recorded in the somatosensory cortex and corresponding animal movements (same experiment as the one shown in Figure 8A-C). A representative ΔF/F trace recorded from the SR area delineated in Figure 8A (upper) and the respective raw (middle) as well as binary (lower) animal movement signals, generated as described in Methods. Arrowheads mark muscle twitches.

resting states, we separated them by transition periods, including one second before the movement onset, and three seconds after the end of the movement. Taking transition period as a safe boundary between resting and motion states helps to prevent any misinterpretation of the Ca^{2+} signal due to slow dynamics of Ca^{2+} indicator dye (GCamP6f) used in this study (Chen et al., 2013).

Overall, the 3-day-old mice moved only 32 ± 18.5% of the recording time (Figure 10), thus spending most of the time in a state with no detectable motion. This result is consistent with our earlier data described in ref (Adelsberger et al., 2005).

Frequency of spontaneous Ca^{2+} signals in the neonatal mouse cortex

To analyze the spatial pattern of spontaneous activity, we first calculated pixel-based frequency maps (see the Methods for details) of activities recorded during the motion and the resting periods (Figure 11). Surprisingly, the pixel-based frequency maps differed dramatically between the two behavioral states, showing spatially distributed activity during the motion period and a prominent activation of posterior cortical areas during the resting period (Figure 11A). Moreover, these distinct spatial patterns were remarkably conserved across experimental animals, so that median frequency maps of 7 experimental animals (Figure 11B) looked almost identical to maps of a single animal (e.g., Figure 11A).

Using the respective frequency maps, we calculated frequencies of spontaneous Ca^{2+} signals in the motor, somatosensory, auditory and visual cortices of the right and the left hemispheres during the two behavioral states (Figure 11C). When analyzing the median frequency values of 7 mice (Figure 11C, lower panel), we did

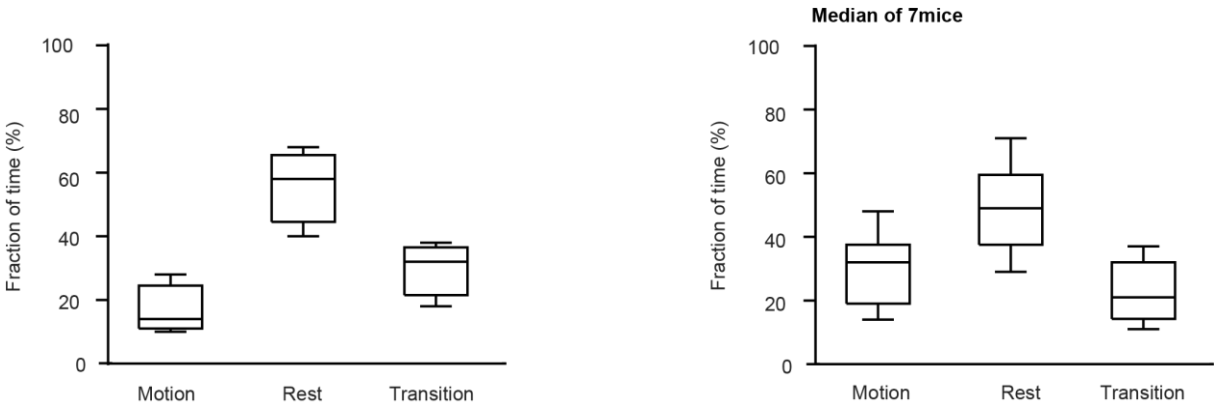

Figure 10. The fraction of time in three different states. Box-and-whisker plots illustrating the fraction of time animals spent in three different states: motion, rest, and transition. The upper plot shows representative data from one mouse (n = 3 10-min-long image series) and the lower plot shows a median of 7 mice. A significant difference was observed between fractions of time spent in 3 different conditions (One-way repeated measure ANOVA followed by Holm-Sidak multiple comparisons test, F1.79*,10.73*=5.35, P = 0.027, here and below a star (*) denotes Greenhaus-Geisser sphericity correction). However, pairwise comparisons using the Holm-Sidak posthoc test did not reach the level of significance.

not observe any differences between the left and the right hemispheres for any condition tested (Repeated Measures ANOVA, $F_{1, 6}= 5x10^{-3}$, p=0.95). Therefore, for further analyses, we averaged data from both hemispheres. During the motion state, the frequency of spontaneous Ca^{2+} signals amounted to 10.64 ± 0.84, 11.97 ± 2.28, 8.42 ± 1.73 and 9.85 ± 2.53 events/min, for motor, somatosensory, auditory and visual cortices, respectively. The corresponding values recorded during the resting state amounted to 0.32 ± 0.37, 0.54 ± 0.48, 0.96 ± 0.83 and 1.44 ± 0.53 events/min. The frequencies of spontaneous Ca^{2+} signals in the given cortical area differed significantly between the motion and resting states (Two-way Repeated Measures ANOVA, $F_{1, 6} = 8.97x10^{2}$, $P < 10^{-3}$), with frequencies observed during the motion state being almost 10 times higher (Figure 11C). In addition, we did observe significant differences in frequencies of spontaneous Ca^{2+} signals among different cortical regions (Two-way Repeated Measures ANOVA $F_{1.53^{*},\ 9.22^{*}} = 14.68$, P = 0.002. Here and below Star (*) denotes Greenhouse-Geisser correction against violations of sphericity). However, pairwise comparisons using the Holm-Sidak posthoc test failed to reach the level of statistical significance.

In summary, the spatial patterns of spontaneous activity in the neonatal cortex differed dramatically between the motion and the resting states, but for a given state, they were impressively stable across the animals. Two types of activity (global and local) were observed during the motion period, whereas at rest, the spontaneous cortical activity was predominantly local.

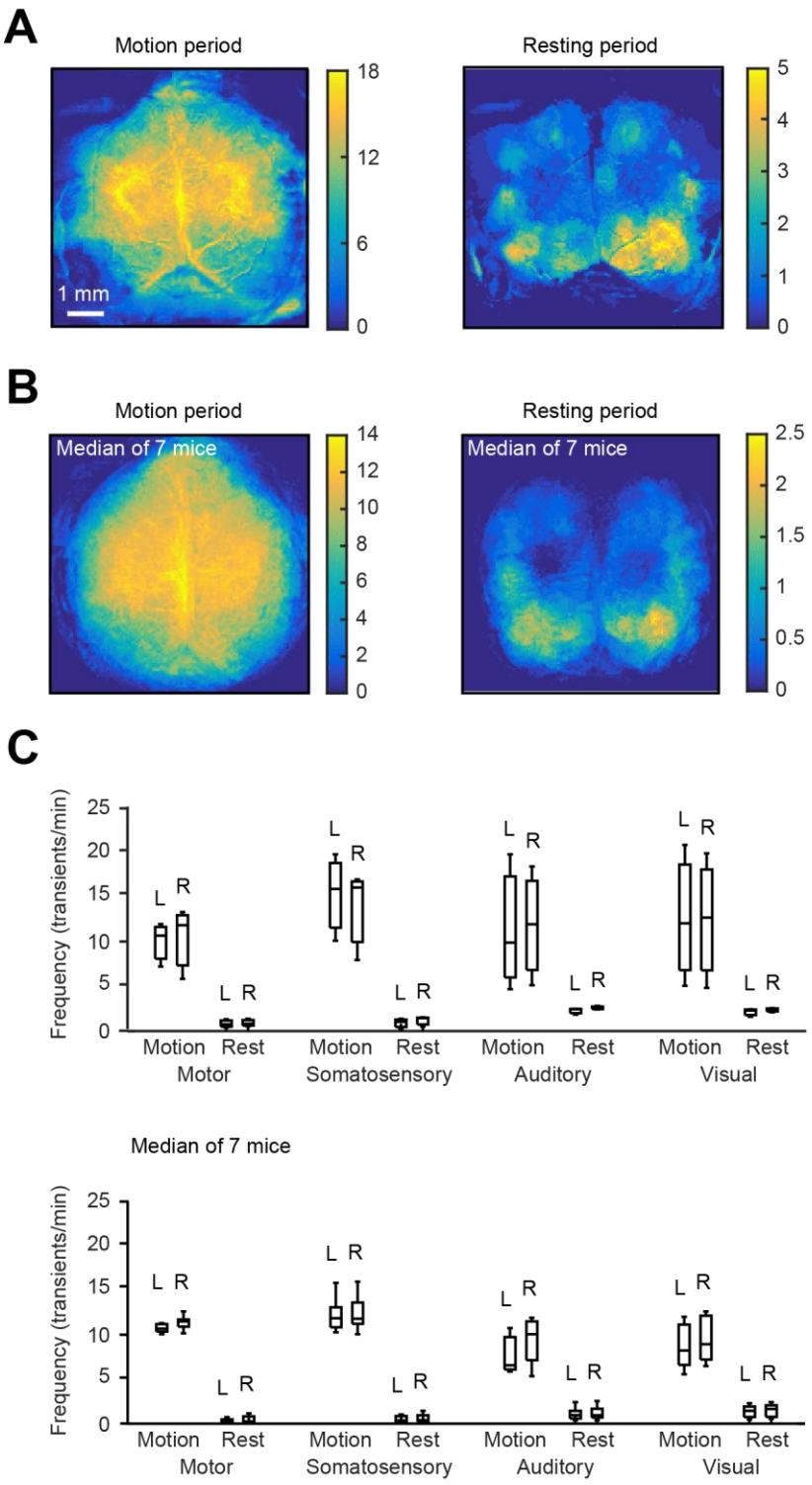

Figure 11. Frequency of spontaneous Ca^{2+} signals in the neonatal mouse cortex. (A) Representative pixel-based frequency maps recorded in a P3 mouse during motion (left panel) and resting (right panel) periods. (B) Same analyses as in A, but each pixel is a median of data obtained in 7 different animals. Here and below before calculating the median, the maps of individual animals were aligned using point set registration technique taking the corresponding blood vessel pattern as a reference. Here and below color-coded bars show frequency of events per minute. Please note different dynamic range used for each image. (C) Box-and-whisker plots illustrating the frequency of spontaneous Ca^{2+} transients within ROIs delineated in Figure 8A (an ROI-specific average of all pixels in a pixel-based frequency map) during motion and resting periods. The upper plot shows data from 3 consecutive 10-min-long image series in a mouse shown in A, and the lower plot shows

Behavioral state-dependent patterns of local cortical activity

In the subsequent analyses, we concentrated on the properties of local activity. To do so, we grouped pixels showing coherent changes in fluorescence intensity into regions of interest (ROIs) using nonnegative matrix factorization algorithm (NMF, see the Methods). Regarding the local activity, the algorithm identified either “single ROIs,” in which all coherently active pixels were immediately adjacent to each other, or “multi-ROIs,” in which coherently active pixels were distributed in patches throughout the dorsal cortex (see the Methods for details). Next, we constructed ROI-based frequency maps of the local spontaneous activity during the motion and the resting periods (Figure 12 A and B; see the Methods for details). Please note that due to the high threshold used during peak detection, some transients contributing to the pixel-based frequency maps were filtered out in analyses shown in Figure 12. On average, coherently active local cortical subregions belonging to either single or multi-ROIs covered the areas of approximately 0.2 mm^2 (Figure 13), and the size of these areas was similar during different behaviors (rest: 0.21 ± 0.06, generalized movements: 0.17 ± 0.03, muscle twitches: 0.18 ± 0.06). However, the resulting ROI-based frequency maps differed dramatically between the motion and rest (Figure 12A). During the motion period, the activity was mostly localized to the somatosensory and a lesser extent motor cortex, whereas at rest it was predominantly found in the visual and auditory cortices as well as a rim of lateral cortical areas likely including temporal and parietal cortices. Noteworthy, these distinct activity patterns were highly conserved across experimental animals (Figure 12B).

To quantify this difference, we calculated spatial correlation coefficients (Lewis, 1995) for ROI-based frequency maps recorded during either the same or different behavioral state. First, we compared the maps calculated for three 10-min-long consecutive recordings in the same animal (Figure 12C) and then compared the median values obtained in 7 mice (Figure 12D). For all animals tested, spatial correlation coefficients were high for “within the state” comparison and much lower when comparing the maps across the different states. From a statistical point of view (Figure 12D), the coefficients were highest during the motion state and somewhat lower during the resting state, whereas the comparison between motion and rest produced correlation coefficients that were close to 0.

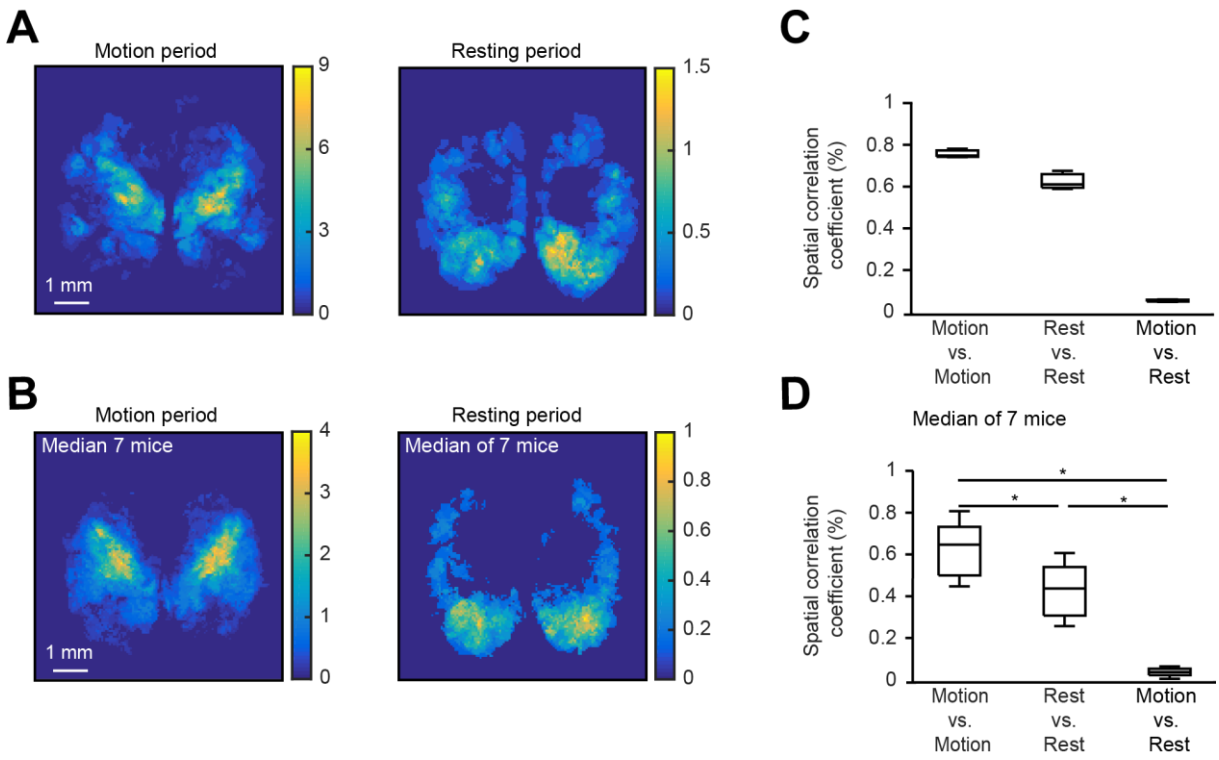

Figure 12 ROI-based frequency maps of local activity. (A) Representative frequency maps based on ROI analysis using nonnegative matrix factorization algorithm recorded in a P3 mouse during motion (left panel) and resting (right panel) time periods. (B) Same analyses as in A, but each pixel is a median of data obtained in 7 different animals. (C) Box-and-whisker plot illustrating spatial correlation coefficients within and between maps obtained during motion and resting time periods (3 maps, each representing a 10-min-long image series recorded in a mouse shown in A). (D) Box-and-whisker plot illustrating medians (per mouse) of spatial correlation coefficients within and between maps obtained during motion and resting time periods. Obtained values are significantly different (One-way repeated measure ANOVA followed by Holm-Sidak multiple comparisons test, $F_{1.6*,9.62*}=71.12$, $P < 0.001$, motion vs. rest: $P = 0.001$, the other two comparisons: $P < 0.001$).

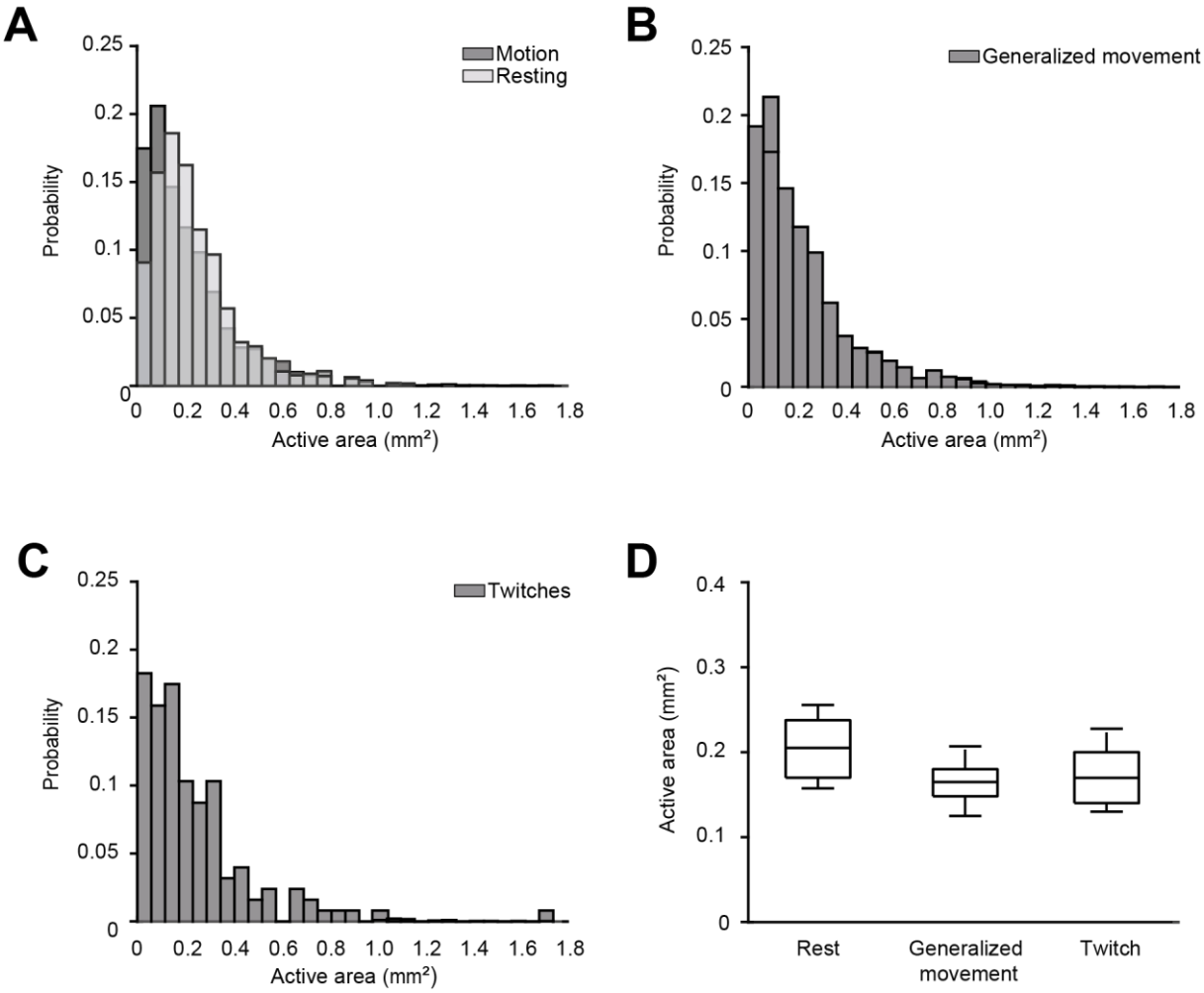

Figure 13 Sizes of coherently active areas contributing to local cortical activity. (A) Normalized histograms of the size of areas active during motion and resting periods, respectively. (B) Normalized histogram of the size of areas active during generalized movements. (C) Normalized histogram of the size of areas active during muscle twitches. (D) Box-and-whisker plot showing median (per mouse) sizes of areas active during the three above mentioned states (in total n = 8621 areas from 6 mice). As shown by the One-way Repeated Measure ANOVA (F1.13*, 5.65* = 3.76, P = 0.1, *denotes Greenhaus-Geisser sphericity correction), the sizes are not significantly different.

The differences between the three groups were statistically significant (One-way Repeated Measure ANOVA $F_{2, 12} = 71.12$, $P < 10^{-3}$ followed by Holm-Sidak multiple comparisons test; motion vs. rest $P = 10^{-3}$ and $P < 10^{-3}$ for the two remaining comparisons). The almost inverse spatial maps of the local activity during the two behavioral states suggest that regions involved in generation and propagation of this spontaneous activity are tightly controlled in a state-dependent manner.

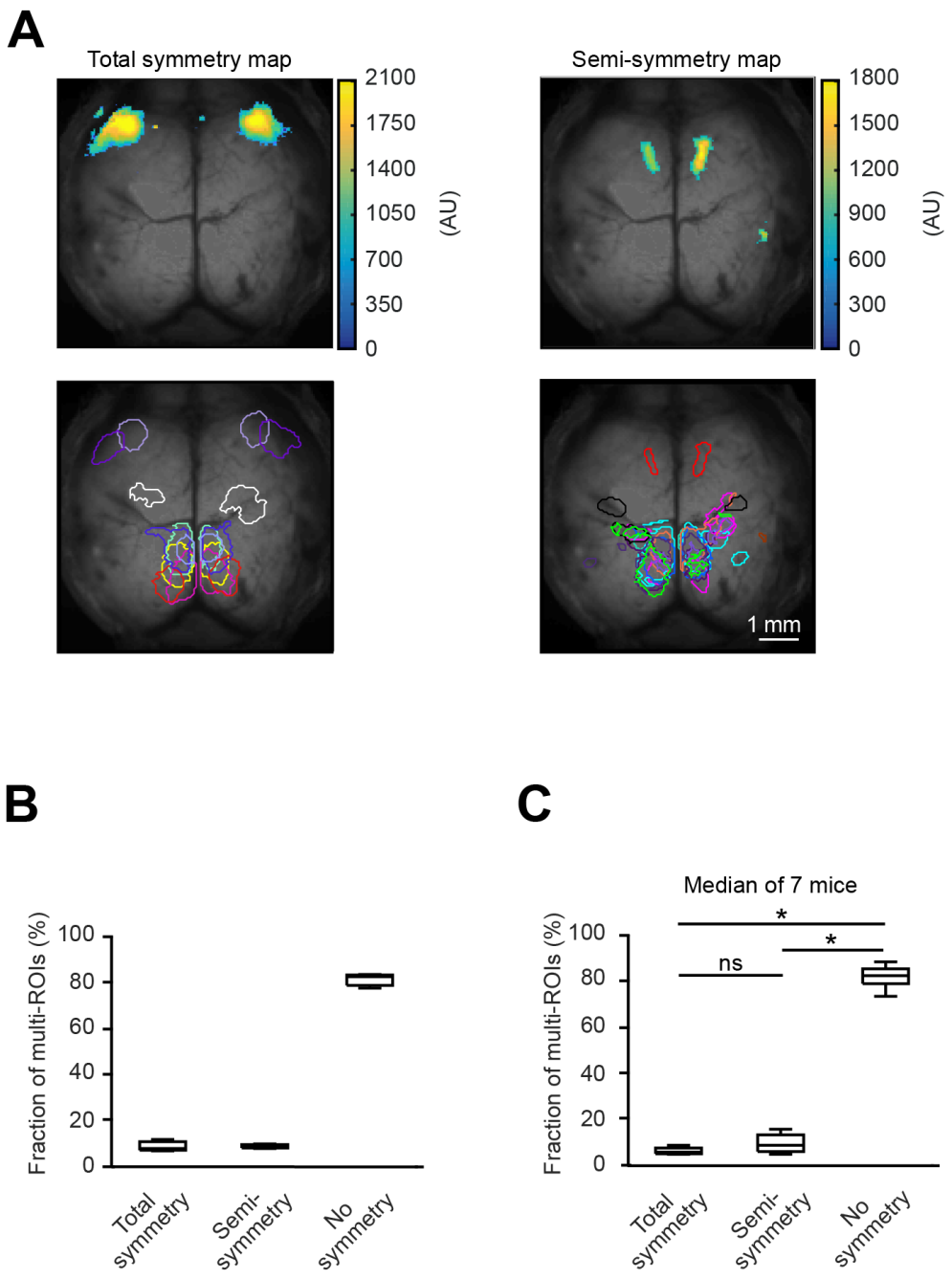

Figure 14 Hemisphere-symmetric neuronal activity in the neonatal mouse cortex. (A) Representative active subregions belonging to one multi-ROI filter (upper) as well as symmetry maps (lower) projected on a grayscale image of P3 mouse cortex. Upper panels: fluorescence signals are color-coded with warmer colors indicating higher signal intensity. Lower panels: different colors delineate multi-ROIs, each satisfying the total (left panel) or semi- (right panel) symmetry criterion (see Methods). (B) Box-and-whisker plot illustrating the median fractions of multi-ROIs in three distinct categories: total, semi- and no symmetry (3 consecutive 10-min-long image series recorded in a mouse shown in A). (C) Same analyses as in B illustrating the median data obtained in 7 different animals. Obtained values are significantly different (One-way repeated measure ANOVA F1.26*,7.56*=625.7, $P < 0.001$). Holm-Sidak multiple comparisons test provides following values: semi-symmetry vs. no symmetry $P < 0.001$, total symmetry vs. no symmetry $P < 0.001$.

Hemispheric asymmetry of the local cortical activity

Next, we used the multi-ROI filters to analyze whether the patterns of coherent spontaneous activity were hemisphere-symmetric (Figure 14). To do so, for each recording we constructed the total symmetry map (containing only hemisphere-symmetric ROIs) and the semi-symmetry map (containing at least one pair of hemisphere-symmetric ROIs, see the Methods) and compared these maps across the animals and the behavioral states.

In general, only 6 ± 2.4% of all multi-ROIs showed a stringent hemispheric symmetry (Figure 14A-C). Another 9 ± 7.25% of multi-ROIs were partially symmetric, whereas 83 ± 6.5 % were totally asymmetric. The vast majority (73 ± 22.7%) of totally symmetric ROIs was observed during the motion period, and only some 10.3 ± 14% of the symmetric activity patterns happened at rest (Figure 15A, C and D). Similar results were obtained for semi-symmetry maps, with 75 ± 29% of respective activity patterns observed during the motion and 12 ± 28% observed during the resting period (Figure 15B, E and F).

Regions contributing to hemisphere-symmetric cortical activity in the neonatal mouse cortex differ between behavioral states

Subsequently, we asked whether regions contributing to hemisphere-symmetric neuronal activity differ between the two behavioral states. For both total and semi-symmetry maps, the fraction of active pixels amounted to less than 22% of all imaged cortical pixels (Figure 16A-D).

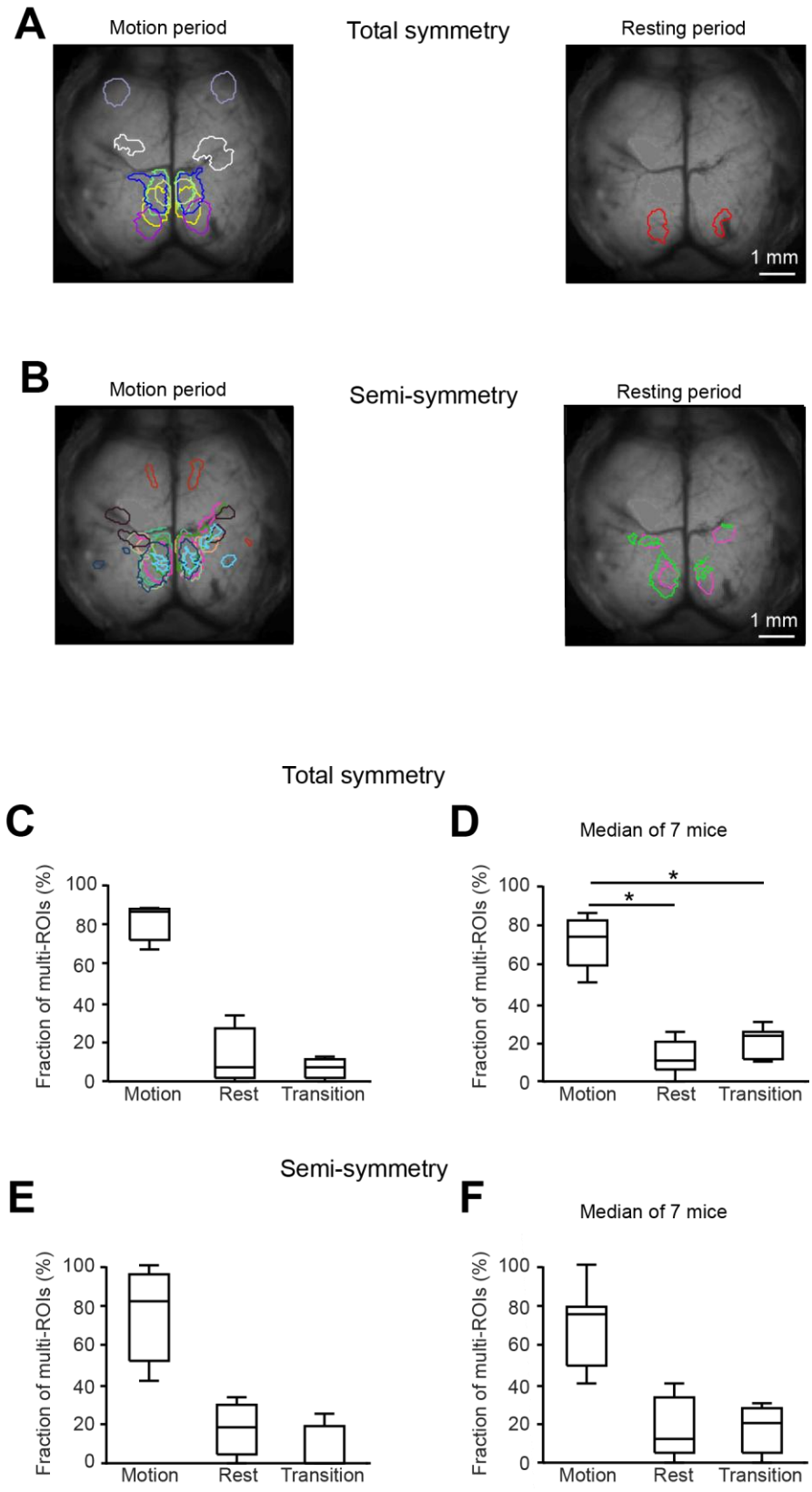

Figure 15 State-dependent hemisphere-symmetric neuronal activity in the neonatal mouse cortex. (A) Representative total symmetry maps recorded during motion (left panel) and resting (right panel) periods. Different colors delineate multi-ROIs, each satisfying the total symmetry criterion. (B) Similar maps as in A but here colors delineate multi-ROIs, each satisfying the semi-symmetry criterion. (C) Box-and-whisker plot showing the median fractions of symmetric multi-ROIs during the three periods: motion, rest, and transition (3 consecutive 10-min-long image series recorded in a mouse shown in A). (D) Same analyses as in C illustrating the median data obtained

in 7 different animals. Obtained values are significantly different (One-way repeated measure ANOVA F1.5*,9.02*=44.65, P < 0.001). Holm-Sidak multiple comparisons test provides following values: motion vs. rest P = 0.001, motion vs. transition P = 0.001. (E) Box-and-whisker plot showing the median fractions semi-symmetric multi-ROIs during the three periods: motion, rest, and transition (3 consecutive 10-min-long image series recorded in a mouse shown in A, B). (F) Same analyses as in E illustrating the median data obtained in 7 different animals.

Still, the fraction of pixels active during the motion period (17.2 ± 3.9% and 21 ± 11.1%, for total and semi-symmetry maps, respectively) was significantly higher than the fraction of pixels active at rest (2.5 ± 5.9% and 7 ± 21.3%; Paired student's t-test; total symmetry: motion vs. rest, $t_5 = 7$, $P < 10^{-3}$; semi-symmetry: motion vs. rest, $t_5 = 5.68$, $P = 2x10^{-3}$). Although we did identify some anatomical regions involved in totally- and semi-symmetric activities during both behavioral states (the most prominent being the retrosplenial cortex, marked with an arrow in Figure 16B), in general, the regions involved in these kinds of activity differed between the resting and motion periods. Thus, for the total symmetry maps (Figure 16E), there were virtually no pixels active both during motion and rest (0 ± 8%). For the semi-symmetry maps, 11 ± 41.75% of pixels active during motion were also active at rest (Figure 16F).

Taken together, this data documents a profound hemispheric asymmetry of spontaneous neuronal activity in the neonatal brain. This lack of symmetry is likely due to the immature corpus callosum (Son et al., 2017), known to coordinate synchronous patterns of activity between hemispheres (David A. McVea, Murphy, & Mohajerani, 2016). At the same time, we show that in the minority of cases hemisphere-symmetric activity patterns do occur and identify the retrosplenial cortex as a region, frequently involved in such type of activity during both the movement and the resting periods.

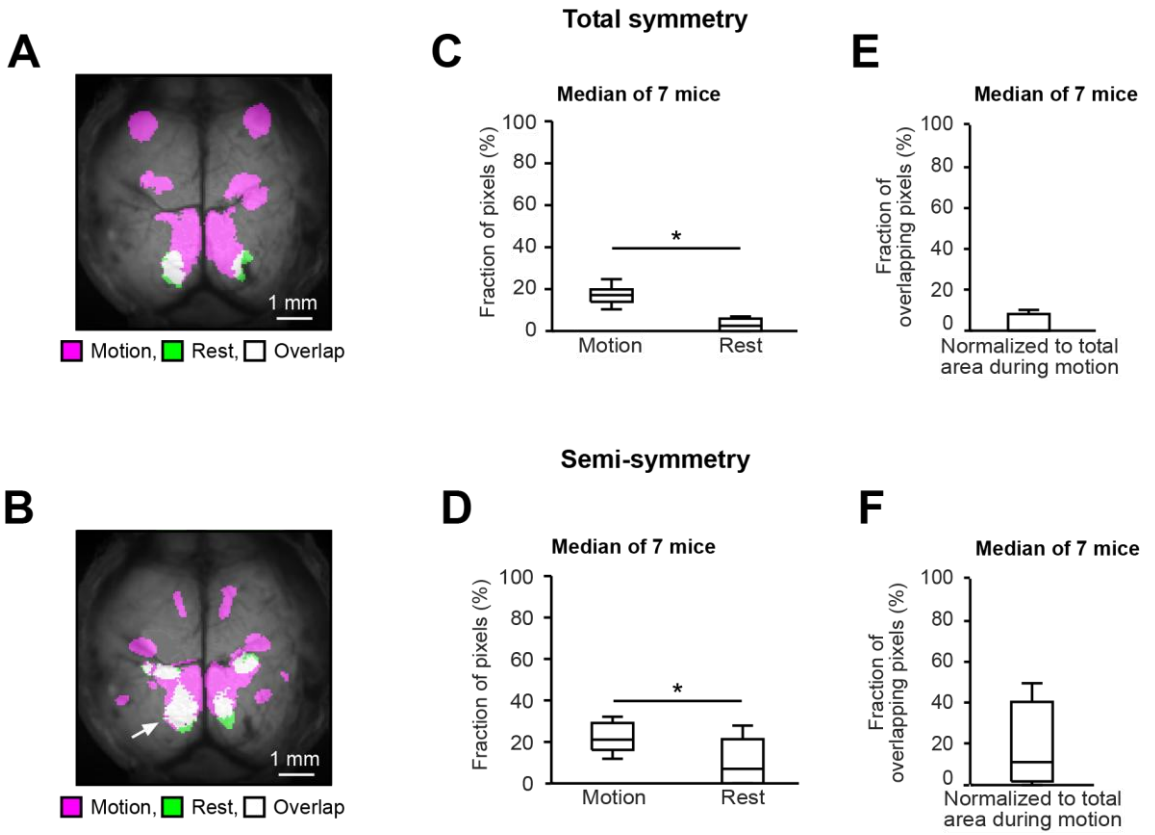

Figure 16 Regions contributing to hemisphere-symmetric cortical activity in the neonatal mouse cortex differ between behavioral states. (A) Spatial representation of the overlap between total symmetry maps recorded during motion and resting time periods in a P3 mouse. Purple color indicates the area active during the motion period, green color marks the area active during the resting period and white color shows the overlapping area. (B) The same representation as in A but for the semi-symmetry map obtained in the same experimental animal. The arrow points to the retrosplenial cortex. For display purpose, an experiment with a prominent overlap is shown. (C) Box-and-whisker plot showing the number of pixels belonging to the total symmetry map during motion (purple area) and rest (green area), as median (per mouse) fractions of the total number of imaged cortical pixels (n = 7 mice). Obtained values are significantly different (paired Student's t-test, t5 = 7, P < 0.001). (D) The same analyses as in C but for the areas contributing to the semi-symmetry map. Obtained values are significantly different (paired Student's t-test, t5 = 5.68, P = 0.002). (E) Box-and-whisker plot showing median (per mouse) numbers of pixels belonging to the white area (as in A) normalized to the number of pixels belonging to the purple area (n = 7 mice). (F) The same analyses as in E but for the areas contributing to the semi-symmetry map.

Behavioral state-specific maps of simultaneously active cortical subregions

Multi-ROI filters, automatically provided by nonnegative matrix factorization algorithm, contain synchronously active group of pixels. Taking this, we investigated simultaneous active regions during the movement and the resting states. First, we determined the anatomical location of all multi-ROI subregions using the map

similar to the one shown in Figure 8A but including, also, the retrosplenial cortex (Figure 17A). Subsequently, we constructed the state-dependent maps (see the Methods for details), in which each edge connected brain regions, which were consistently simultaneously active in a behavioral state-specific manner within and across experimental animals (Figure 17B-D). The circles indicate instances in which pairs of active subregions of a multi-ROI were located within the same anatomical region.

Independent from the behavioral state, the simultaneously active subregions were found either close to each other (e.g. within the same anatomical region) or up to several mm apart, as exemplified in Figure 17 B and C. In general, the center-to-center distances between simultaneously active subregions ranged between 0.33 and 5.78 mm (1^{st} – 99^{th} percentile), with median of 2.12 ± 0.39 mm. When taking 3 mm as a border between the short- and the long-range activities, the majority of activity patterns (72.2 ± 16.52%) belonged to the short-range activity (n = 6 mice; Figure 18). When comparing median (per mouse) distances between the subregions active during the motion and the resting states, no significant difference was found (motion: 2.13 ± 0.41 mm, rest: 2.23 ± 0.16 mm; Wilcoxon signed-rank test z = 0.52, P= 0.69, n=6 mice; Figure 18B). However, consistent with the general activity pattern described in Figure 12, the regions contributing to the simultaneous activity map differed dramatically between the motion and the resting state. During the motion state, the synchronously active subregions were mostly located in the anterior (motor, somatosensory) cortical regions, shifting to the posterior (e.g., visual) cortical regions during the resting state (Figure 17C). Interestingly, auditory and retrosplenial cortices contributed to the map of simultaneous activity during both behavioral states.

During the motion period; however, the retrosplenial cortex was predominantly active together with the motor cortex, while during the resting state, it was predominantly active together with the visual cortex. The median simultaneous activity map obtained for all recorded mice (n = 6; Figure 17D) assured the solidity of the described above findings.

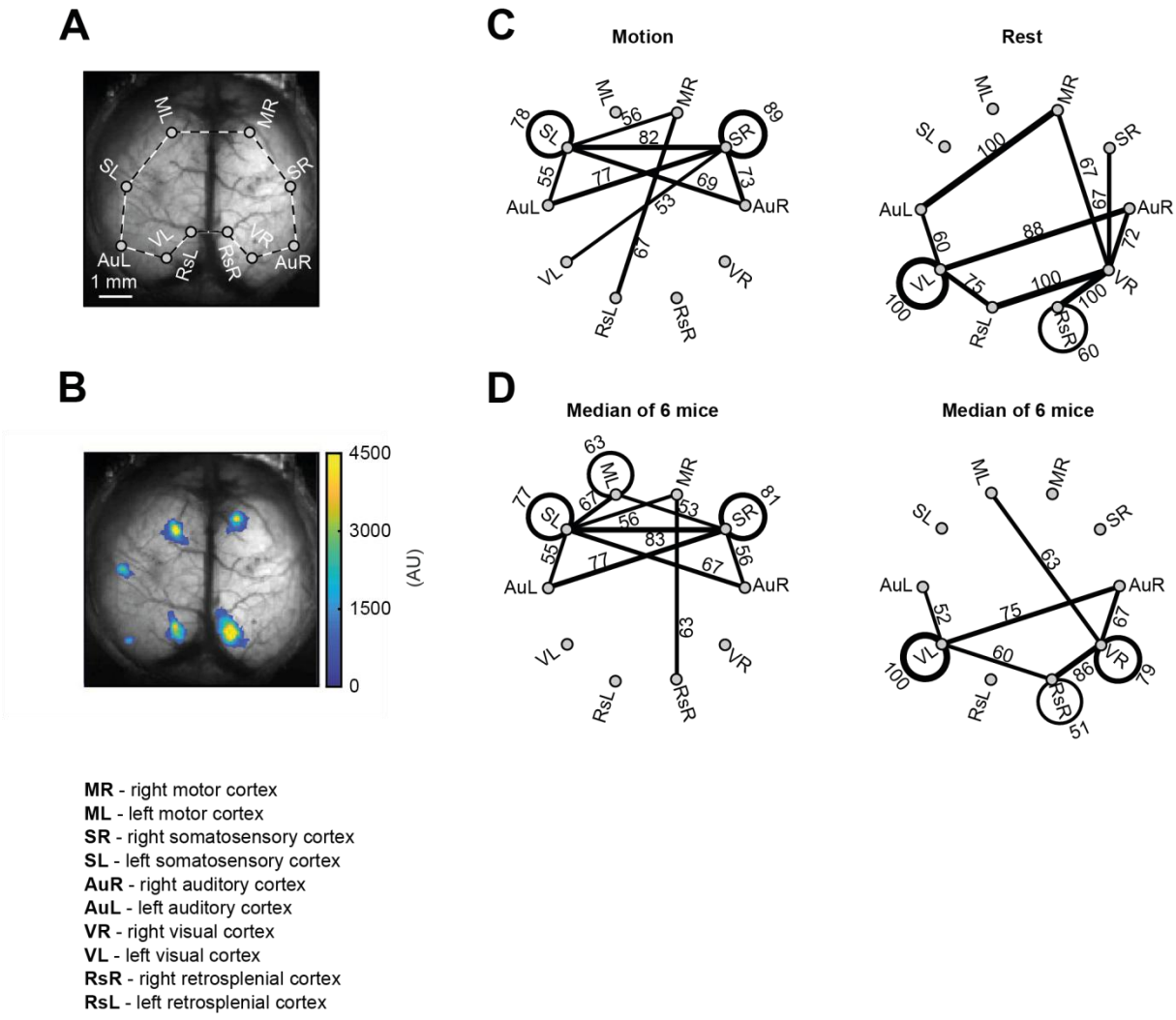

Figure 17 Map of simultaneously active cortical regions. (A) Top view on a P3 mouse cortex. Dots are positioned within the respective cortical areas of interest, listed under the image. (B) Representative active subregions belonging to one multi-ROI filter, projected on a grayscale image of P3 mouse cortex. Fluorescence signals are color-coded with warmer colors indicating higher signal intensity. (C) Representative multi-ROI-based maps of simultaneously active regions recorded during the two different behavioral states: motion and rest (3 consecutive 10-min-long image series). Nodes represent cortical areas pre-defined in A and edges between two nodes depict cases when two simultaneously active subregions are located in the two cortical areas. Similarly, circles depict cases when two simultaneously active subregions are located in the same cortical area. Numbers along the edges (or circles) represent the normalized number of transients, i.e. the fractions of cases occurring either during the motion (left) or the rest (right), respectively (D) Same analyses as in B but illustrating median data obtained in 6 different mice. Only the edges and circles with values of ≥50% are shown.

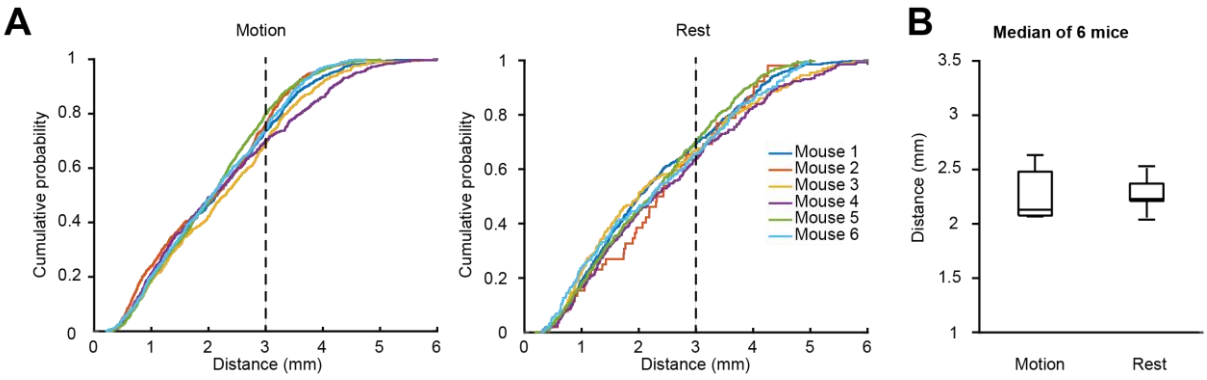

Figure 18 Distance between simultaneously active cortical subregions. (A) Cumulative probability functions of all pairwise distances between the centers of simultaneously active subregions belonging to the same multi-ROI filters during motion (left panel) and resting (right panel) periods. Distributions obtained in different mice (n = 6) are shown in different colors. (B) Box-and-whisker plot showing median (per mouse) distances between the centers of coherently active subregions (n = 6 mice).

Waves of activity propagating through the neonatal cortex

So far, when describing the observed activity patterns, we have mostly considered their spatial dimension. With the temporal dimension added (see the Methods for details), the observed neonatal activity patterns represented waves of activity either propagating in a given direction (e.g., Figure 19A, left panel) or waxing and waning in magnitude and spatial area involved without any apparent movement of the wave's center of mass (so-called stationary waves). Of all propagating waves observed, the majority (81 ± 25%) was recorded during the motion period with a significantly smaller fraction of waves (19 ± 25%; Paired student's t-test, $t_5 = 3.21$, P = 0.02) being recorded at rest (Figure 19B, left panel). A similar trend was also observed for stationary waves (Figure 19B, right panel) but the difference did not reach the level of statistical significance (motion: 81 ± 36%, rest: 19 ± 34%).

Next, we characterized the fractions of waves invading different anatomical regions (i.e., motor, somatosensory, auditory, visual and retrosplenial cortices) of the right and the left hemispheres during the two behavioral states. For both propagating and stationary waves, we did not observe any differences between the left and the right

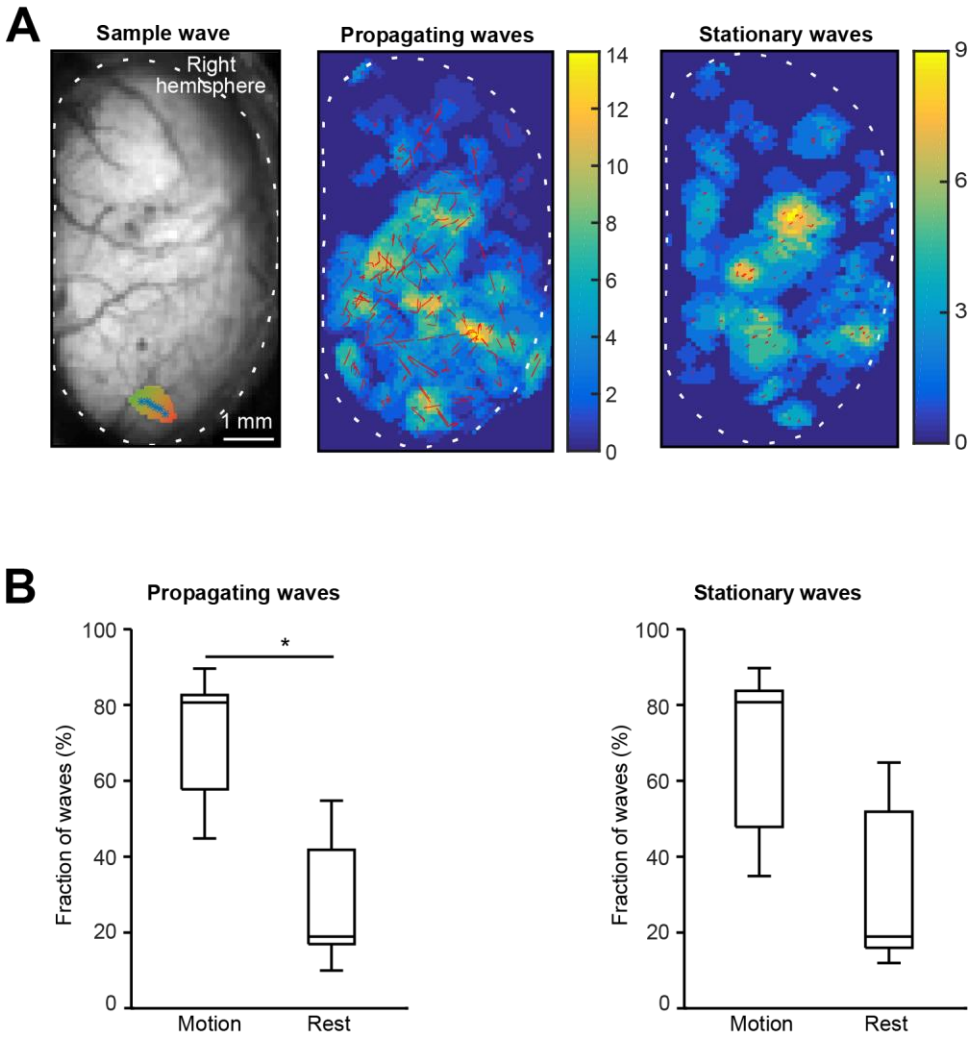

Figure 19 Stationary and propagating Ca^{2+} waves in the neonatal mouse cortex. (A) The left panel shows a top view on the right hemisphere of a P3 mouse cortex with an example of a propagating wave. The direction of movement is color-coded from green to red. Blue stars depict the location of the center of mass in each frame (see the Methods). Broken line delineates the contour of the brain area imaged in this experiment. The middle panel is a superposition of propagating waves recorded in this animal in 6 min. False colors reflect the number of waves each pixel was involved into (see the scale bar), the corresponding center of mass trajectories are depicted as red lines. The right panel is a superposition of stationary waves recorded in this animal in 6 min. Red lines depict the center of mass trajectories of each wave. (B) Box-and-whisker plots showing median (per mouse) fractions of propagating (left panel) and stationary (right panel) waves happening during motion and rest, respectively (n = 6 mice). For each mouse, the number of propagating waves during the motion (or rest) was normalized to the number of all propagating waves recorded. Similar normalization procedure was used for stationary waves.

hemisphere for any condition tested (Repeated Measures ANOVA; Figure 20A: $F_{1, 5}$= 3.53, p=0.12; Figure 20B: $F_{1, 5}$= $2.83x10^{-4}$, p=0.98; Figure 20C: $F_{1, 5}$= 4.13, p=0.1; Figure 20D: $F_{1, 5}$= 0.001, p=0.98).

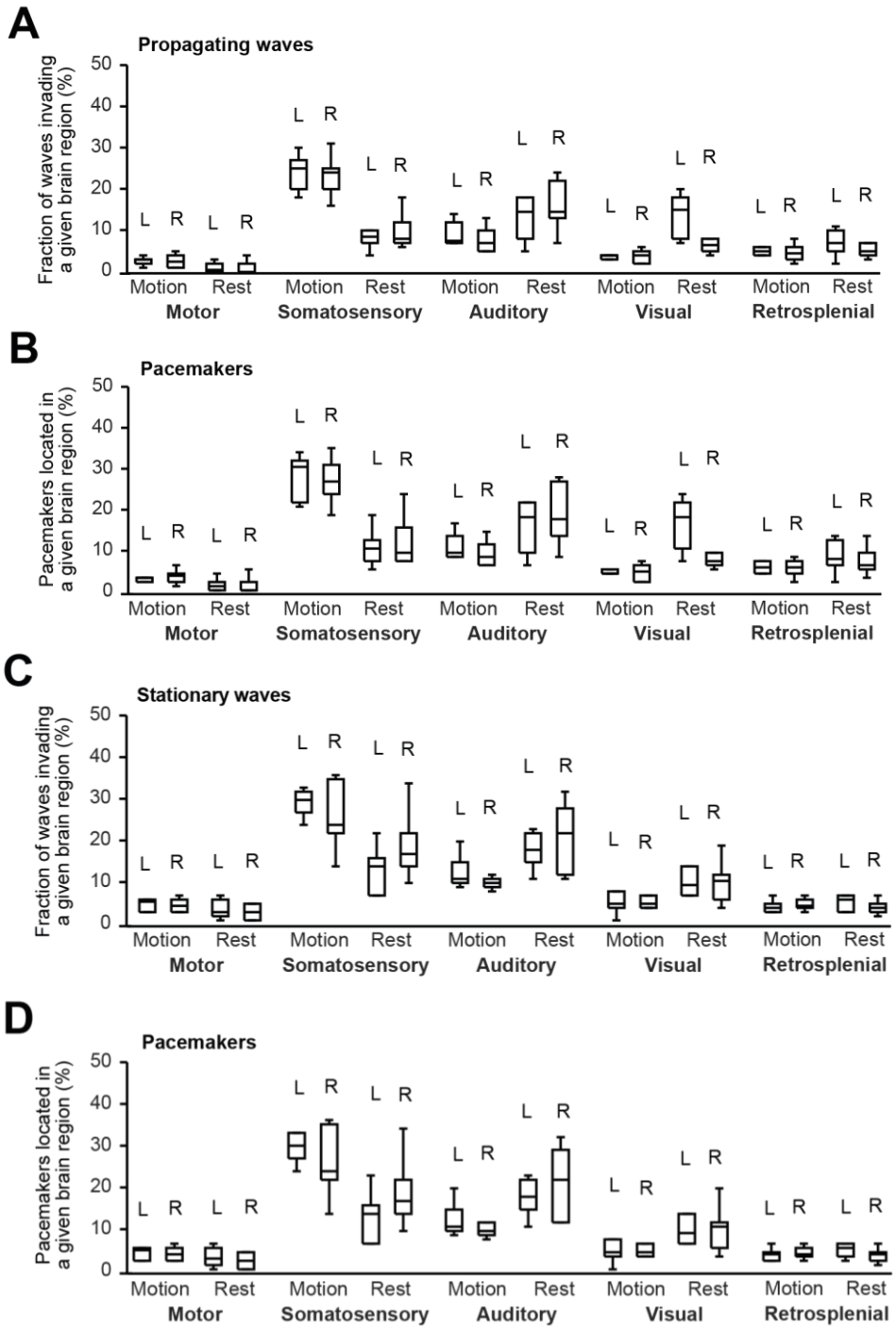

Figure 20 Stationary and propagating waves in the neonatal mouse cortex. (A and C) Median (per mouse) fractions of propagating (A) and stationary (C) waves invading the respective cortical areas in the left (L) and the right (R) hemisphere. (B and D) Similar analyses as in A and C but illustrating fractions of pacemakers for propagating (B) and stationary (D) waves located in the given cortical area (n = 6 mice).

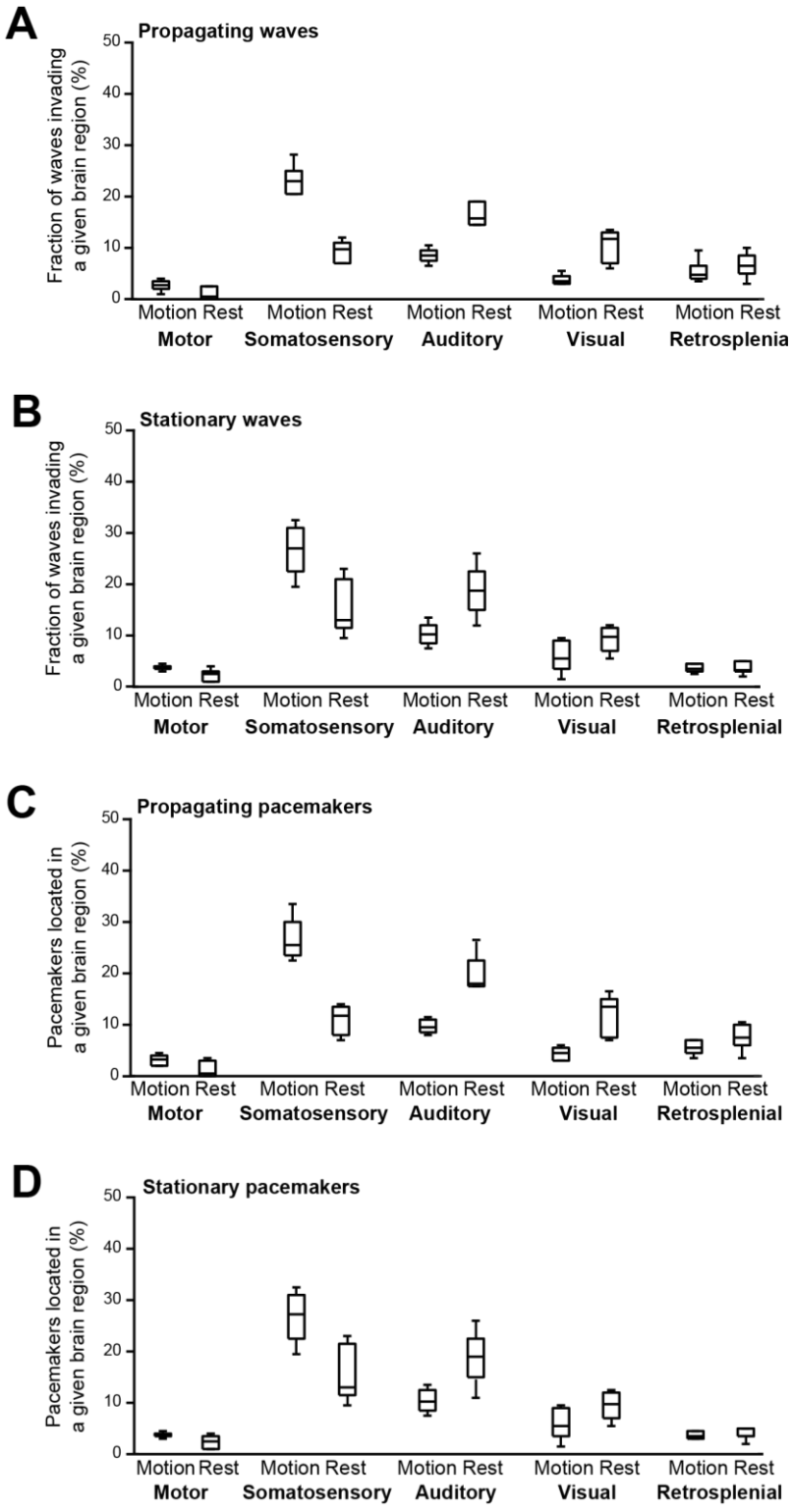

Figure 21 Region dependent stationary and propagating Ca^{2+} waves in the neonatal mouse cortex. (A and B) Box-and-whisker plots showing averaged between the two hemispheres median (per mouse) fractions of propagating (A) and stationary (B) waves invading the respective cortical areas. (C and D) Similar analyses as in A and B but illustrating median (per mouse) fractions of pacemakers for propagating (C) and stationary (D) waves located in the given cortical region (n = 6 mice). To calculate the fraction of propagating/stationary waves in a given cortical region during the motion/rest the number of propagating waves observed in this region during this particular state was normalized to the number of all propagating waves detected in this state.

Therefore, for further analyses, we averaged the data from both hemispheres (Figure 21). During the motion state the highest fraction of both propagating (23 ± 4.5%, Figure 21A) and stationary (27 ± 8.5%, Figure 21B) waves invaded the somatosensory cortex, whereas at rest the waves mostly invaded somatosensory, auditory and visual cortices (9.75 ± 4%, 15.75 ± 4.5%, 11.75 ± 6% for propagating and 13 ± 9.5%, 18.75 ± 7.5%, 9.75 ± 4.5% for stationary waves, respectively). Next, we analyzed locations of pacemakers (defined as described in the Methods), initiating a given type of activity. During the motion state, the pacemakers were

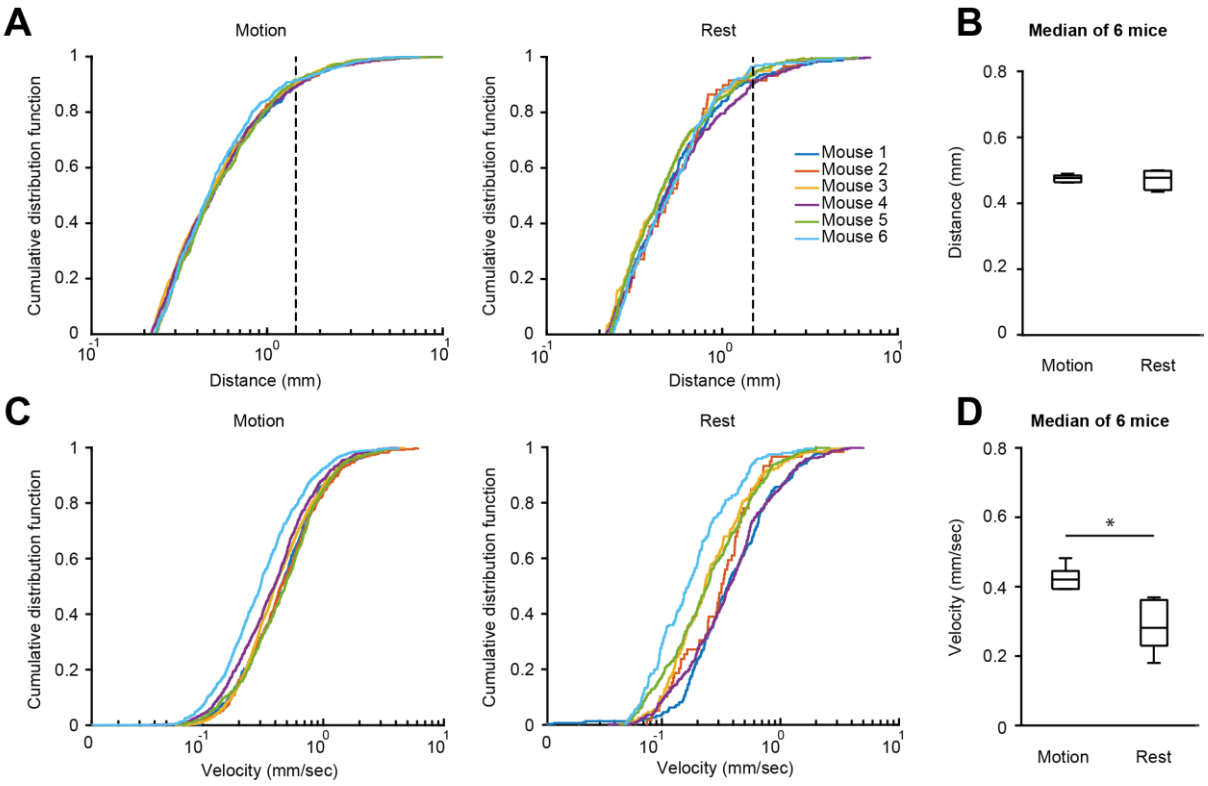

Figure 22 Distance and velocity of propagating waves. (A) Cumulative probability functions of all distances traveled by propagating waves during motion (left panel) and resting (right panel) time periods. Distributions obtained in different mice (n = 6) are shown in different colors. The dashed line marks the empiric border (1.5 mm) between the waves propagating over the short and the long distances. X-axes are shown in logarithmic scale. (B) Box-and-whisker plot showing median (per mouse) distances traveled by propagating waves during motion and resting time periods (paired Student's t-test, t5 = 0.34, P = 0.75). (C) Cumulative probability functions of all average apparent velocities of propagating waves recorded during motion (left panel) and resting (right panel) time periods. X-axes are shown in logarithmic scale. (D) Box-and-whisker plot showing median (per mouse) apparent velocity of propagating waves during motion and resting states. Obtained values are significantly different (paired Student's t-test, t5 =4.3, P = 0.008).

mostly located in the somatosensory cortex (25.5 ± 6.5% of pacemakers for propagating (Figure 21C) and 27.25 ± 8.5% for stationary (Figure 21D) waves, respectively). During the resting state the pacemakers were mostly distributed between the somatosensory, auditory and visual cortices (11.75 ± 5.5%, 18 ± 5%, 13.5 ± 7.5% of pacemakers for propagating and 13 ± 10%, 19 ± 7.5%, 9.75 ± 5% for stationary waves, respectively). The overall similarity in the distributions of waves invading a given cortical area and their pacemakers suggests that the majority of waves spread over rather short distances.

To test this assumption, we analyzed the distances traveled by the centers of mass of all propagating waves in our dataset. In general, the propagating waves spread over distances of 0.22 - 4.76 mm (1^{st} – 99^{th} percentile), with the median of 0.47 ± 0.02 mm (n = 6 mice, not differentiating between motion and rest). When taking 1.5 mm as a border between the waves propagating over short- vs. long distances, the majority (91 ± 2% of waves) spread over the short distances. The apparent center of mass velocity ranged from 0.06 till 3.5 mm/s (1^{st} – 99^{th} percentile), with the median of 0.38 ± 0.05 mm/s (n = 6 mice). When comparing the properties of waves propagating during the motion and the resting states (Figure 22), there was no significant difference between the distributions of median (per mouse) propagation distances (motion: 0.47 ± 0.02 mm, rest: 0.47 ± 0.06 mm; Paired student's t-test t_5 = 0.34, P = 0.75, n = 6 mice; Figure 22B) but the respective propagation velocities (Figure 22D) were significantly different (motion: 0.42 ± 0.05 mm/s, rest: 0.28 ± 0.13 mm/s; Paired student's t-test t_5 = 4.31, P = 0.01, n = 6 mice).

Thus, the spontaneous neuronal activity in the dorsal cortex of neonates contains a rich and spatially complex pattern of both stationary and propagating waves. The majority of the propagating waves are associated with the animal’s movement, whereas stationary waves seem to occur with roughly similar incidence during the

movement and the resting periods. Interestingly, the waves of both types are triggered predominantly in the somatosensory or auditory cortices.

Functional connectivity map of early cortical activity

Spontaneous correlated neuronal activity is believed to represent a functional template for activity-dependent maturation of intracortical connections and the refinement of functional units underlying information processing at adulthood (Hanganu-Opatz, 2010; Luhmann et al., 2016). To test for functional connectivity between the different cortical regions (Figure 23), we used a sparse inverse covariance matrix estimation algorithm (see the Methods for details). This analysis was shown to measure the direct association between the two brain regions removing the contributions caused by global or third-party effects (for more details on the method we refer the reader to ref. (Huang et al., 2010)).

The level of the sparseness of the algorithm's outcome was controlled by the tuning parameter γ. Thanks to the monotone property of the algorithm used (Huang et al., 2010), increasing γ monotonically increases the level of the sparseness of cortical connectivity at the expense of weaker connections. As shown in Figure 23 (upper panel), at low values of γ, we have observed direct functional connections within and in-between of many anatomical regions, defined as illustrated in Figure 17A. However, the majority of these connections were weak because they disappeared with an increasing γ (Figure 23, lower panel). The remaining strong connections emphasized the short-range intraregional connectivity as well as behavioral state-specific long-range connections between the more anterior regions during motion. Interestingly, the method identified the strong and direct functional link between the ipsilateral retrosplenial and somatosensory cortices, present during both behavioral states, as well as some prominent state-specific connections (Figure 23).

Together, these data reveal that in neonatal mice, functionally connected cortical subregions are distributed through the entire dorsal cortical surface. The connectivity pattern is characterized by dense short-range connections, linking different subregions of the given anatomical area, as well as sparse long-range connections. The latter differ substantially between the resting and the motion state. These differences are highly conserved across experimental animals, thus reflecting typical activity patterns of the neonatal brain.

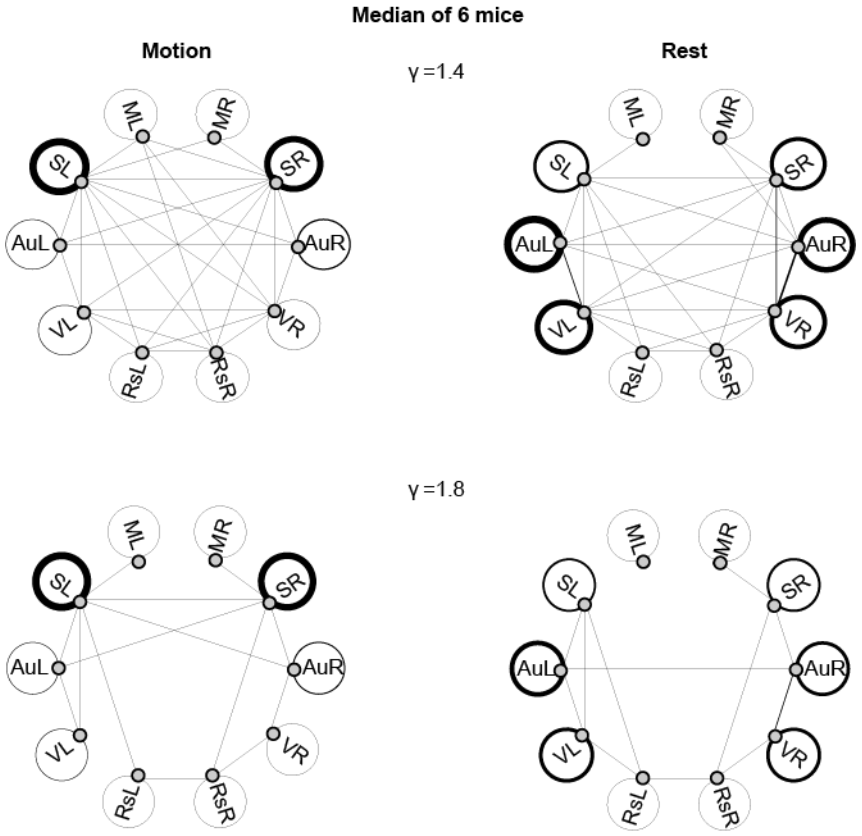

Figure 23 Functional connectivity map. Direct connectivity maps calculated for motion (left panels) and resting (right panels) periods with two different values of γ (see the Methods). Nodes represent cortical regions of interest predefined in Figure 17A and edges between the two nodes show the direct connectivity between the two cortical regions. Edge thickness represents the median strength of connections between the two cortical regions. Similarly, circles depict connectivity within the given cortical region and thickness of each circled line shows the median strength of connections in this cortical region. Median of data obtained from 6 different animals.

Discussion

The current study provides a unifying view on the spontaneous neuronal activity in the dorsal cortex of neonates. It shows that in the awake state this activity is represented by a complex mixture of local events, often limited to a given cortical region, and large scale fluorescence changes (global events) (Figure 8B). Analysis of spatial pattern of spontaneous activities (Figure 11A), showed dramatic difference between the two behavioral states, where complex mixture of local and large scale fluorescence changes covering the most recorded area of the cortex during the motion period and a prominent activation of posterior cortical areas during the resting period. Interestingly, these large scale fluorescence changes occurred after the onset of the motion (Figure 8C, blue dash line and gray line). Moreover, the existence of the large scale fluorescence change during the motion period was also observed in C57BL/6 mice (data is not shown) which do not express the Ca^{2+} indicator GCaMP6. Therefore, this suggests that the observed large scale fluorescence changes are unspecific and one possible reason for observing such events might be the motion artifact which was not fully corrected during preprocessing step.

The spatially-restricted Ca^{2+} transients represented the predominant type of activity at rest. These findings identify spatially-restricted Ca^{2+} signals as the main type of spontaneous network activity in the neonatal cortex. In-depth characterization of this type of activity revealed (i) its rich spatio-temporal structure comprising distributed patches of coherent activity in spatial as well as propagating and stationary waves in spatio-temporal domains, (ii) its genuine hemispheric asymmetry in the spatial domain, (iii) its ontogenetically-conserved and non-overlapping behavioral state-specific spatial maps, and (iv) the surprising existence of long-range functional connections, often involving the retrosplenial cortex, at the developmental stage at which anatomical long-range connections are either not yet developed or immature

(Hartung, Brockmann, Pöschel, De Feo, & Hanganu-Opatz, 2016; Tagawa & Hirano, 2012).

Strikingly, local cortical activity patterns recorded during the motion and the resting states turned out to be almost inverse with very little overlap between the two. During the motion activity was restricted to the somatosensory-motor area (compare active area in Figure 12A to the map of the adult mouse brain in ref.(Vanni, Chan, Balbi, Silasi, & Murphy, 2017)), consistent with the cumulative knowledge derived from earlier reports (An et al., 2014; Rustem Khazipov et al., 2004; D. A. McVea et al., 2012; Tiriac et al., 2012) as well as with recent data showing that active wake movements suppress spontaneous neural activity in the visual cortex of neonatal rats(Mukherjee, Yonk, Sokoloff, & Blumberg, 2017). In contrast, during the rest local activity completely spared the above areas being restricted to the visual, auditory and retrosplenial cortex as well as lateral cortical areas, such as, for example, the temporal cortex, known for its movement-independent spontaneous network activity (Adelsberger et al., 2005).

Such sharp segregation of the activity patterns is surprising also in view of the fact that during the developmental stage studied here, both motion and rest are behaviorally heterogeneous. Indeed, motion comprises both generalized movements happening during wakefulness, and muscle twitches mainly observed during active sleep (Seelke et al., 2005; Tiriac, Del Rio-Bermudez, & Blumberg, 2014). Similarly, the resting period might also include both quiet wakefulness and quiet sleep. Because under our experimental conditions the overall duration of muscle twitches comprised only 5 - 16% of the total movement time, the described here motion-related activity pattern is dominated by the one caused by wake-related generalized movements. Still, it is consistent with the activity pattern, seen by others during spontaneous muscle twitches (D. A. McVea et al., 2012; Tiriac et al., 2012).

Thus, under conditions when animal's limbs are free to interact with each other and the supporting surface, both kinds of self-generated movements discussed above (predominantly wake-related generalized movements: current study, muscle twitches: refs. (Rustem Khazipov et al., 2004; D. A. McVea et al., 2012; Tiriac et al., 2014, 2012) cause a robust and predominantly reafferent neuronal activity in the somatosensory-motor area of the cortex. Whereas muscle twitch-related activity is spatially confined and organized in a somatotopic manner (Rustem Khazipov et al., 2004; D. A. McVea et al., 2012), activity patterns associated with wake-related generalized movements often cause global cortical signals.

Considering the cortical areas involved in the behavioral state-specific patterns of spontaneous network activity, our work has identified the unique binding role of the retrosplenial cortex, an area (i) involved in both motion- and rest-related ongoing activities, especially in their hemisphere-symmetric subtypes and (ii) maintaining strong long-range functional connections with many other studied cortical regions. Although the consensus on the precise function of this cortical area is still missing, evidence from both human and animal studies points to its role in spatial navigation, visuospatial integration and hippocampus-related learning and memory (Czajkowski et al., 2014; Vann, Aggleton, & Maguire, 2009). Moreover, in humans, retrosplenial cortex was shown to be active during the resting brain state, thus belonging to the so-called "default mode network" (Vann et al., 2009). Whereas many areas belonging to the default mode network are known to decrease their activity upon engagement into a cognitive task (Anticevic et al., 2012), this is not the case for the retrosplenial cortex, which increases its activity, for example, during tests of spatial navigation and autobiographical memory retrieval (Vann et al., 2009). Of special interest is also the fact that although areas involved into default mode network vary across different age groups, this is not the case for the retrosplenial cortex, which

represents its inherent part from early infancy through adolescence into adulthood (Vann et al., 2009). Thus, both in humans and now also in mice from early on the retrosplenial cortex seems to represent a functional bridge between the default mode network active at rest and task- or movement-specific neural networks coordinating ongoing activity in the sensorimotor system. To do so, the retrosplenial cortex engages into behavioral state-specific coherent activity with the respective cortical areas: visual cortex at rest and somatosensory cortices during motion. The long-range nature of the latter functional connections is in marked contrast with the developmental state of the immature P3 mouse brain, in which long-range anatomical connections are immature (Hartung et al., 2016; Tagawa & Hirano, 2012). Interestingly, a recent study of the ferret visual cortex also discovered long-range (albeit intra-regional) functional connections at the developmental stage (P21 - 22 in ferret) similar to the one studied here (G. B. Smith et al., 2018). To explain their data, the authors presented a dynamical rate network model, which in a regime of strongly heterogeneous local connectivity and moderate input modulation produces pronounced long-range correlations, similar to the ones observed in an experiment. Noteworthy, the spatial structure of the correlated activity produced by the model was fairly robust against changes in input drive strength, in agreement with author's data that long-range correlations persisted in the immature cortex even after silencing the main driving input (i.e., spontaneous retinal waves reaching the visual cortex via the lateral geniculate nucleus (G. B. Smith et al., 2018)). The described above findings suggest that neonatal brain utilizes local spontaneously active inputs to drive the correlated activity of distant cortical regions, thus providing the template for activity- and Ca^{2+}-dependent growth and branching of long-range axonal projections (Tagawa & Hirano, 2012). Indeed, the anatomical studies in adult rodents suggest that retrosplenial cortex, to stay with this example, is directly linked

with anterior cingulate, motor and visual cortices (Vann et al., 2009; Yamawaki, Radulovic, & Shepherd, 2016).

Together, the knowledge obtained in the present study binds different region-specific activity patterns described so far by us and others into a single consistent picture. Besides the suggested role of this activity in synchronizing the development of cortical microcircuits (Golshani et al., 2009), our data suggest its involvement in macrocircuit development by showing that neonatal cortical activity is capable of generating both long-range functional coherence between selected cortical areas and global activity engaging the entire cortex. Moreover, it identifies both stationary and propagating waves as putative building blocks of the endogenous brain activity in neonates and sets the stage for future inactivation studies probing the exact function of this complex activity pattern for activity-dependent cortical wiring during the precritical period(Feller & Scanziani, 2005).

References

Ackman, J. B., & Crair, M. C. (2014a). Role of emergent neural activity in visual map development. *Current Opinion in Neurobiology*, *24*(1), 166–175. https://doi.org/10.1016/j.conb.2013.11.011

Ackman, J. B., & Crair, M. C. (2014b). Role of emergent neural activity in visual map development. *Current Opinion in Neurobiology*, *24*(December 2013), 166–175. https://doi.org/10.1016/j.conb.2013.11.011

Adelsberger, H., Garaschuk, O., & Konnerth, A. (2005). Cortical calcium waves in resting newborn mice. *Nature Neuroscience*, *8*(8), 988–990. https://doi.org/10.1038/nn1502

Allen Institute for Brain Science. (2015). Allen Brain Atlas: Mouse Connectivity.

Allen, T., Mouse, D., Atlas, B., Developing, A., Brain, M., Atlas, R., & Puelles, L. (2010). Technical White Paper : Allen Developing Mouse Brain Reference Atlas, (March), 1–12.

Allene, C., Cattani, A., Ackman, J. B., Bonifazi, P., Aniksztejn, L., Ben-Ari, Y., & Cossart, R. (2008). Sequential Generation of Two Distinct Synapse-Driven Network Patterns in Developing Neocortex. *Journal of Neuroscience*, *28*(48), 12851–12863. https://doi.org/10.1523/jneurosci.3733-08.2008

An, S., Kilb, W., & Luhmann, H. J. (2014). Sensory-Evoked and Spontaneous Gamma and Spindle Bursts in Neonatal Rat Motor Cortex. *Journal of Neuroscience*, *34*(33), 10870–10883. https://doi.org/10.1523/JNEUROSCI.4539-13.2014

Anticevic, A., Cole, M. W., Murray, J. D., Corlett, P. R., Wang, X. J., & Krystal, J. H. (2012). The role of default network deactivation in cognition and disease. *Trends in Cognitive Sciences*. https://doi.org/10.1016/j.tics.2012.10.008

Antón-Bolaños, N., Sempere-Ferràndez, A., Guillamón-Vivancos, T., Martini, F. J., Pérez-Saiz, L., Gezelius, H., … López-Bendito, G. (2019). Prenatal activity from thalamic neurons governs the emergence of functional cortical maps in mice. *Science*, *7617*(May), eaav7617. https://doi.org/10.1126/science.aav7617

B. L. Finlay & R. B. Darlington. (1995). Linked regularities in the development and evolution of mammalian brains. *Science*, *268*(5217), 1578–1584.

Badalà, F., Nouri-mahdavi, K., & Raoof, D. A. (2012). Retinal waves coordinate patterned activity throughout the developing visual system. *Nature*, *490*(7419), 219–225. https://doi.org/10.1038/jid.2014.371

Bandeira, F., Lent, R., & Herculano-Houzel, S. (2009). Changing numbers of neuronal and non-neuronal cells underlie postnatal brain growth in the rat. *Proceedings of the National Academy of Sciences*, *106*(33), 14108–14113. https://doi.org/10.1073/pnas.0804650106

Berens, P., Freeman, J., Deneux, T., Chenkov, N., McColgan, T., Speiser, A., … Bethge, M. (2018). Community-based benchmarking improves spike rate inference from two-photon calcium imaging data. *PLoS Computational Biology*, *14*(5), 1–13. https://doi.org/10.1371/journal.pcbi.1006157

Berry, M. W., Browne, M., Langville, A. N., Pauca, V. P., & Plemmons, R. J. (2007). Algorithms and applications for approximate nonnegative matrix factorization. *Computational Statistics and Data Analysis*, *52*(1), 155–173. https://doi.org/10.1016/j.csda.2006.11.006

Beutner, D., & Moser, T. (2001). The presynaptic function of mouse cochlear inner hair cells during development of hearing. *The Journal of Neuroscience : The Official Journal of the Society for Neuroscience*, *21*(13), 4593–4599. Retrieved from http://www.ncbi.nlm.nih.gov/pubmed/11425887

Blumberg, M. (2010). Beyond dreams: do sleep-related movements contribute to

brain development? *Frontiers in Neurology*, *1*(November), 1–10. https://doi.org/10.3389/fneur.2010.00140

Brockmann, M. D., Pöschel, B., Cichon, N., & Hanganu-Opatz, I. L. (2011). Coupled Oscillations Mediate Directed Interactions between Prefrontal Cortex and Hippocampus of the Neonatal Rat. *Neuron*, *71*(2), 332–347. https://doi.org/10.1016/j.neuron.2011.05.041

Chen, T.-W., Wardill, T. J., Sun, Y., Pulver, S. R., Renninger, S. L., Baohan, A., … Kim, D. S. (2013). Ultrasensitive fluorescent proteins for imaging neuronal activity. *Nature*, *499*(7458), 295–300. https://doi.org/10.1038/nature12354

Clause, A., Kim, G., Sonntag, M., Weisz, C. J. C., Vetter, D. E., Rubsamen, R., & Kandler, K. (2014). The Precise Temporal Pattern of Prehearing Spontaneous Activity Is Necessary for Tonotopic Map Refinement. *Neuron*, *82*(4), 822–835. https://doi.org/10.1016/j.neuron.2014.04.001

Cohen, M. R., & Kohn, A. (2011). Measuring and interpreting neuronal correlations. *Nature Neuroscience*, *14*(7), 811–819. https://doi.org/10.1038/nn.2842

Corlew, R., Bosma, M. M., & Moody, W. J. (2004). Spontaneous, synchronous electrical activity in neonatal mouse cortical neurones. *The Journal of Physiology*, *560*(Pt 2), 377–390. https://doi.org/10.1113/jphysiol.2004.071621

Corne´J. Kros, J. P. R. & A. R. (2004). Expression of apotassium current in inner hair cells duringdevelopment of hearing inmice. *Nature*, *428*(March), 1–4. https://doi.org/10.1038/nature02371.1.

Crépel, V., Aronov, D., Jorquera, I., Represa, A., Ben-Ari, Y., & Cossart, R. (2007). A Parturition-Associated Nonsynaptic Coherent Activity Pattern in the Developing Hippocampus. *Neuron*, *54*(1), 105–120. https://doi.org/10.1016/j.neuron.2007.03.007

Czajkowski, R., Jayaprakash, B., Wiltgen, B., Rogerson, T., Guzman-Karlsson, M.

C., Barth, A. L., … Silva, A. J. (2014). Encoding and storage of spatial information in the retrosplenial cortex. *Proceedings of the National Academy of Sciences*, *111*(23), 8661–8666. https://doi.org/10.1073/pnas.1313222111

de Villers-Sidani, E., Chang, E. F., Bao, S., & Merzenich, M. M. (2007). Critical Period Window for Spectral Tuning Defined in the Primary Auditory Cortex (A1) in the Rat. *Journal of Neuroscience*, *27*(1), 180–189. https://doi.org/10.1523/jneurosci.3227-06.2007

Dimitrova, N., Zamudio, J. R., Jong, R. M., Soukup, D., Resnick, R., Sarma, K., … Jacks, T. (2017a). Sensorineural Deafness and Seizures in Mice Lacking Vesicular Glutamate Transporter 3. *PLoS ONE*, *32*(7), 736–740. https://doi.org/10.1371/journal.pone.0178059

Dimitrova, N., Zamudio, J. R., Jong, R. M., Soukup, D., Resnick, R., Sarma, K., … Jacks, T. (2017b). Spontaneous Discharge Patterns in Cochlear Spiral Ganglion Cells Prior to the Onset of Hearing in Cats. *PLoS ONE*, *32*(7), 736–740. https://doi.org/10.1371/journal.pone.0178059

Dombeck, D. A. (2007). Imaging large scale neural activity with cellular resolution in awake mobile mice. *Neuron*, *56*(1), 43–57.

Eldawlatly, S. (2013). On The Use of Dynamic Bayesian Networks in Reconstructing Functional Neuronal Networks from Spike Train Ensembles, *71*(2), 233–236. https://doi.org/10.1038/mp.2011.182.doi

Eran A. Mukamel. (2009). Automated analysis of cellular signals from large-scale calcium imaging data. *Neuron*, *63*(6), 747–760. https://doi.org/10.1016/j.neuron.2009.08.009.Automated

Feller, M. B., & Scanziani, M. (2005). A precritical period for plasticity in visual cortex. *Current Opinion in Neurobiology*. https://doi.org/10.1016/j.conb.2005.01.012

Friedman, J., Hastie, T., & Tibshirani, R. (2008). Sparse inverse covariance estimation with the graphical lasso. *Biostatistics*, *9*(3), 432–441. https://doi.org/10.1093/biostatistics/kxm045

Friston, K. J. (2011). Functional and Effective Connectivity: A Review. *Brain Connectivity*. https://doi.org/10.1089/brain.2011.0008

Fujisawa, S., Amarasingham, A., Harrison, M. T., & Buzsáki, G. (2008). Behavior-dependent short-term assembly dynamics in the medial prefrontal cortex. *Nature Neuroscience*, *11*(7), 823–833. https://doi.org/10.1038/nn.2134

Galli, & Maffei. (1988). Spontaneous Impulse Activity of Rat Retinal Ganglion Cells in Prenatal Life Localizaion of an Arg-Gly-Asp Recognition Site Within an Integrin Adhesion Receptor. *Science*, *242*, 21–22.

Garaschuk, O., Hanse, E., & Konnerth, A. (1998). Developmental profile and synaptic origin of early network oscillations in the CA1 region of rat neonatal hippocampus. *Journal of Physiology*, *507*(1), 219–236. https://doi.org/10.1111/j.1469-7793.1998.219bu.x

Garaschuk, O., Linn, J., Eilers, J., & Konnerth, A. (2000). Large-scale oscillatory calcium waves in the immature cortex. *Nature Neuroscience*, *3*(5), 452–459. https://doi.org/10.1038/74823

Garofalo, M., Nieus, T., Massobrio, P., & Martinoia, S. (2009). Evaluation of the performance of information theory-based methods and cross-correlation to estimate the functional connectivity in cortical networks. *PLoS ONE*, *4*(8). https://doi.org/10.1371/journal.pone.0006482

Geal-Dor, M., Freeman, S., Li, G., & Sohmer, H. (1993). Development of hearing in neonatal rats: Air and bone conducted ABR thresholds. *Hearing Research*, *69*(1–2), 236–242. https://doi.org/10.1016/0378-5955(93)90113-F

Gee, J. M., Smith, N. A., Fernandez, F. R., Economo, M. N., Brunert, D., Rothermel,

M., … Tvrdik, P. (2014). Imaging Activity in Neurons and Glia with a Polr2a-Based and Cre-Dependent GCaMP5G-IRES-tdTomato Reporter Mouse. *Neuron*. https://doi.org/10.1016/j.neuron.2014.07.024

Ginat, D. T., & Gupta, R. (2014). Advances in Computed Tomography Imaging Technology. *Annual Review of Biomedical Engineering*, *16*(1), 431–453. https://doi.org/10.1146/annurev-bioeng-121813-113601

Glowatzki, E., & Fuchs, P. A. (2002). Transmitter release at the hair cell ribbon synapse. *Nature Neuroscience*, *5*(2), 147–154. https://doi.org/10.1038/nn796

Glueckert, R., Wietzorrek, G., Kammen-Jolly, K., Scholtz, A., Stephan, K., Striessnig, J., & Schrott-Fischer, A. (2003). Role of class D L-type Ca2+ channels for cochlear morphology. *Hearing Research*, *178*(1–2), 95–105. https://doi.org/10.1016/S0378-5955(03)00054-6

Golshani, P., Goncalves, J. T., Khoshkhoo, S., Mostany, R., Smirnakis, S., & Portera-Cailliau, C. (2009). Internally Mediated Developmental Desynchronization of Neocortical Network Activity. *Journal of Neuroscience*, *29*(35), 10890–10899. https://doi.org/10.1523/jneurosci.2012-09.2009

Greenberg, D. S., & Kerr, J. N. D. (2009). Automated correction of fast motion artifacts for two-photon imaging of awake animals. *Journal of Neuroscience Methods*, *176*(1), 1–15. https://doi.org/10.1016/j.jneumeth.2008.08.020

Grienberger, C., & Konnerth, A. (2012). Imaging Calcium in Neurons. *Neuron*, *73*(5), 862–885. https://doi.org/10.1016/j.neuron.2012.02.011

Grover, V. P. B., Tognarelli, J. M., Crossey, M. M. E., Cox, I. J., Taylor-Robinson, S. D., & McPhail, M. J. W. (2015). Magnetic Resonance Imaging: Principles and Techniques: Lessons for Clinicians. *Journal of Clinical and Experimental Hepatology*, *5*(3), 246–255. https://doi.org/10.1016/j.jceh.2015.08.001

Hanganu-Opatz, I. L. (2010). Between molecules and experience: Role of early

patterns of coordinated activity for the development of cortical maps and sensory abilities. *Brain Research Reviews*. https://doi.org/10.1016/j.brainresrev.2010.03.005

Hanganu, I. L., Ben-Ari, Y., & Khazipov, R. R. (2006). Retinal waves trigger spindle bursts in the neonatal rat visual cortex. *The Journal of Neuroscience : The Official Journal of the Society for Neuroscience*, *26*(25), 6728–6736. https://doi.org/10.1523/JNEUROSCI.0752-06.2006

Hartung, H., Brockmann, M. D., Pöschel, B., De Feo, V., & Hanganu-Opatz, I. L. (2016). Thalamic and Entorhinal Network Activity Differently Modulates the Functional Development of Prefrontal–Hippocampal Interactions. *The Journal of Neuroscience*, *36*(13), 3676–3690. https://doi.org/10.1523/JNEUROSCI.3232-15.2016

Hirtz, J. J., Boesen, M., Braun, N., Deitmer, J. W., Kramer, F., Lohr, C., … Friauf, E. (2011). Cav1.3 Calcium Channels Are Required for Normal Development of the Auditory Brainstem. *Journal of Neuroscience*, *31*(22), 8280–8294. https://doi.org/10.1523/JNEUROSCI.5098-10.2011

Huang, S., Li, J., Sun, L., Ye, J., Fleisher, A., Wu, T., … Reiman, E. (2010). Learning brain connectivity of Alzheimer's disease by sparse inverse covariance estimation. *NeuroImage*, *50*(3), 935–949. https://doi.org/10.1016/j.neuroimage.2009.12.120

Johnson, S. L., Marcotti, W., & Kros, C. J. (2005). Increase in efficiency and reduction in Ca2+ dependence of exocytosis during development of mouse inner hair cells. *Journal of Physiology*, *563*(1), 177–191. https://doi.org/10.1113/jphysiol.2004.074740

Junek, S., Chen, T. W., Alevra, M., & Schild, D. (2009). Activity correlation imaging: Visualizing function and structure of neuronal populations. *Biophysical Journal*,

96(9), 3801–3809. https://doi.org/10.1016/j.bpj.2008.12.3962

Kandler, K., Clause, A., & Noh, J. (2009). Tonotopic reorganization of developing auditory brainstem circuits. *Nature Neuroscience*, *12*(6), 711–717. https://doi.org/10.1038/nn.2332

Kandler, K., & Katz, L. C. (1998). Coordination of Neuronal Activity in Developing Visual Cortex by Gap Junction-Mediated Biochemical Communication, *18*(4), 1419–1427.

Kelly, J. B., & Sally, S. L. (1988). Organization of auditory cortex in the albino rat: binaural response properties. *Journal of Neurophysiology*, *59*(6), 1756–1769. https://doi.org/10.1152/jn.1988.59.6.1756

Khazipov, R., & Luhmann, H. J. (2006). Early patterns of electrical activity in the developing cerebral cortex of humans and rodents. *Trends in Neurosciences*. https://doi.org/10.1016/j.tins.2006.05.007

Khazipov, R., Minlebaev, M., & Valeeva, G. (2013). Early gamma oscillations. *Neuroscience*, *250*, 240–252. https://doi.org/10.1016/j.neuroscience.2013.07.019

Khazipov, R., Sirota, A., Leinekugel, X., Holmes, G. L., Ben-Ari, Y., & Buzsáki, G. (2004). Early motor activity drives spindle bursts in the developing somatosensory cortex. *Nature*, *432*(7018), 758–761. https://doi.org/10.1038/nature03132

Kirischuk, S., Sinning, A., Blanquie, O., Yang, J.-W., Luhmann, H. J., & Kilb, W. (2017). Modulation of Neocortical Development by Early Neuronal Activity: Physiology and Pathophysiology. *Frontiers in Cellular Neuroscience*, *11*(November), 1–21. https://doi.org/10.3389/fncel.2017.00379

Kirkby, L. A., Sack, G. S., Firl, A., & Feller, M. B. (2013). A role for correlated spontaneous activity in the assembly of neural circuits. *Neuron*.

https://doi.org/10.1016/j.neuron.2013.10.030

Kirmse, K., Kummer, M., Kovalchuk, Y., Witte, O. W., Garaschuk, O., & Holthoff, K. (2015). GABA depolarizes immature neurons and inhibits network activity in the neonatal neocortex in vivo. *Nature Communications*, *6*, 7750. https://doi.org/10.1038/ncomms8750

Ko, H., Cossell, L., Baragli, C., Antolik, J., Clopath, C., Hofer, S. B., & Mrsic-Flogel, T. D. (2013). The emergence of functional microcircuits in visual cortex. *Nature*, *496*(7443), 96–100. https://doi.org/10.1038/nature12015

Lewis, J. P. (Industrial L. & M. (1995). Fast Normalized Cross-Correlation Template Matching by Cross-. *Vision Interface*, *1995*(1), 1–7. https://doi.org/10.1007/s00034-009-9130-7

Liang, H., Hippenmeyer, S., & Ghashghaei, H. T. (2012). A Nestin-cre transgenic mouse is insufficient for recombination in early embryonic neural progenitors. *Biology Open*, *1*(12), 1200–1203. https://doi.org/10.1242/bio.20122287

Lim, J. S. (1989). *Two-Dimensional Signal and Image Processing*. *Englewood Cliffs, NJ, Prentice Hall*.

Lippe, W. R. (1994). Rhythmic spontaneous activity in the developing avian auditory system. *The Journal of Neuroscience : The Official Journal of the Society for Neuroscience*, *14*(3 Pt 2), 1486–1495. Retrieved from http://www.ncbi.nlm.nih.gov/pubmed/8126550

Lipton, a J., Fujiyoshi, H., & Patil, R. S. (1998). Moving target classification and tracking from real-time video. *Proceedings Fourth IEEE Workshop on Applications of Computer Vision WACV98 Cat No98EX201*, *98*(2), 8–14. https://doi.org/10.1109/ACV.1998.732851

Lucas, B. D., & Kanade, T. (1981). An Iterative Image Registration Technique with an Application to Stereo Vision. *Robotics*, *81*(September), 674–679.

https://doi.org/10.1109/HPDC.2004.1323531

Luhmann, H. J. (2016). Review of imaging network activities in developing rodent cerebral cortex *in vivo*. *Neurophotonics*, *4*(3), 031202. https://doi.org/10.1117/1.NPh.4.3.031202

Luhmann, H. J., & Khazipov, R. (2017). Neuronal activity patterns in the developing barrel cortex. *Neuroscience*. https://doi.org/10.1016/j.neuroscience.2017.05.025

Luhmann, H. J., Sinning, A., Yang, J., & Reyes-puerta, V. (2016). Spontaneous Neuronal Activity in Developing Neocortical Networks : From Single Cells to Large-Scale Interactions. *Frontiers in Neural Circuits*, *10*(May), 1–14. https://doi.org/10.3389/fncir.2016.00040

Ma, S., Xue, L., & Zou, H. (2012). Alternating Direction Methods for latent variable Gaussian graphical model selection. *Neural Computation*, *1872*(1), 1840–1872. https://doi.org/10.1162/NECO

Manley, G. (2013). Genetic Influences on Brain Developmental Trajectories on Neuroimaging Studies: From Infancy to Young Adulthood, *71*(2), 233–236. https://doi.org/10.1038/mp.2011.182.doi

McCormick, D. A., Trent, F., & Ramoa, A. S. (1995). Postnatal development of synchronized network oscillations in the ferret dorsal lateral geniculate and perigeniculate nuclei. *The Journal of Neuroscience : The Official Journal of the Society for Neuroscience*, *15*(8), 5739–5752. Retrieved from http://www.ncbi.nlm.nih.gov/pubmed/7643215

McVea, D. A., Mohajerani, M. H., & Murphy, T. H. (2012). Voltage-Sensitive Dye Imaging Reveals Dynamic Spatiotemporal Properties of Cortical Activity after Spontaneous Muscle Twitches in the Newborn Rat. *Journal of Neuroscience*, *32*(32), 10982–10994. https://doi.org/10.1523/JNEUROSCI.1322-12.2012

McVea, D. A., Murphy, T. H., & Mohajerani, M. H. (2016). Large Scale Cortical Functional Networks Associated with Slow-Wave and Spindle-Burst-Related Spontaneous Activity. *Frontiers in Neural Circuits*. https://doi.org/10.3389/fncir.2016.00103

Minlebaev, M., Ben-Ari, Y., & Khazipov, R. (2009). NMDA receptors pattern early activity in the developing barrel cortex in vivo. *Cerebral Cortex*, *19*(3), 688–696. https://doi.org/10.1093/cercor/bhn115

Miri, A., Daie, K., Burdine, R. D., Aksay, E., & Tank, D. W. (2010). Regression-Based Identification of Behavior-Encoding Neurons During Large-Scale Optical Imaging of Neural Activity at Cellular Resolution. *Journal of Neurophysiology*, *105*(2), 964–980. https://doi.org/10.1152/jn.00702.2010

Mostafapour, S. P., Cochran, S. L., Mae Del Puerto, N., & Rubel, E. W. (2000). Patterns of cell death in mouse anteroventral cochlear nucleus neurons after unilateral cochlea removal. *Journal of Comparative Neurology*, *426*(4), 561–571. https://doi.org/10.1002/1096-9861(20001030)426:4<561::AID-CNE5>3.0.CO;2-G

Mukherjee, D., Yonk, A. J., Sokoloff, G., & Blumberg, M. S. (2017). Wakefulness suppresses retinal wave-related neural activity in visual cortex. *Journal of Neurophysiology*, *118*(2), 1190–1197. https://doi.org/10.1152/jn.00264.2017

N., R., B., M., J.L., F., R., G., & M., W. (2018). Longitudinal analysis of developmental changes in electroencephalography patterns and sleep-wake states of the neonatal mouse. *PLoS ONE*, *13*(11), 1–17. https://doi.org/10.1371/journal.pone.0207031 LK - http://sfx.library.uu.nl/utrecht?sid=EMBASE&issn=19326203&id=doi:10.1371%2Fjournal.pone.0207031&atitle=Longitudinal+analysis+of+developmental+changes+in+electroencephalography+patterns+and+sleep-

wake+states+of+the+neonatal+mouse&stitle=PLoS+ONE&title=PLoS+ONE&volume=13&issue=11&spage=&epage=&aulast=Rensing&aufirst=Nicholas&auinit=N.&aufull=Rensing+N.&coden=POLNC&isbn=&pages=-&date=2018&auinit1=N&auinitm=

Narahashi, T. (2004). Principles of Electrophysiology: An Overview. *Current Protocols in Toxicology*, 1–11. https://doi.org/10.1002/0471140856.tx1110s17

Neher, E., & Sakaba, T. (2008). Multiple roles of calcium ions in the regulation of neurotransmitter release. *Neuron*, *59*(6), 861–872. https://doi.org/10.1016/j.neuron.2008.08.019

Olshevsky, V., Tyrtyshnikov, E., Golyandina, N. E., & Usevich, K. D. (2010). 2D-Extension of Singular Spectrum Analysis: Algorithm and Elements of Theory. In *Matrix Methods: Theory, Algorithms and Applications*. https://doi.org/10.1142/9789812836021_0029

Oppenheim, A. V, & Schafer, R. W. (2009). Discrete Time Signal Processing (2nd version). *Book*.

Orlandi, J. G., Stetter, O., Soriano, J., Geisel, T., & Battaglia, D. (2014). Transfer entropy reconstruction and labeling of neuronal connections from simulated calcium imaging. *PLoS ONE*, *9*(6). https://doi.org/10.1371/journal.pone.0098842

Owens, D. F., & Kriegstein, A. R. (1998). Patterns of intracellular calcium fluctuation in precursor cells of the neocortical ventricular zone. *The Journal of Neuroscience : The Official Journal of the Society for Neuroscience*, *18*(14), 5374–5388. Retrieved from http://www.ncbi.nlm.nih.gov/pubmed/9651220

Ozden, I., Lee, H. M., Sullivan, M. R., & Wang, S. S.-H. (2008). Identification and Clustering of Event Patterns From In Vivo Multiphoton Optical Recordings of Neuronal Ensembles. *Journal of Neurophysiology*, *100*(1), 495–503.

https://doi.org/10.1152/jn.01310.2007

Paans, A. M. J. (2004). Positron emission tomography. *Molecular Imaging & Biology*, *6*(2), 72–73. https://doi.org/10.1016/j.mibio.2004.01.013

Pachitariu, M., Stringer, C., Dipoppa, M., Schröder, S., Rossi, L. F., Dipoppa, M., … Harris, K. D. (2016). Suite2p : beyond 10 , 000 neurons with standard two-photon microscopy. *BioRxiv*, 1–30. https://doi.org/10.1101/061507

Petersen, A., Simon, N., & Witten, D. (2017). Scalpel: Extracting neurons from calcium imaging data. *Annals of Applied Statistics*, *12*(4), 2430–2456. https://doi.org/10.1214/18-AOAS1159

Petersen, C. C. H. (2007). The functional organization of the barrel cortex. *Neuron*, *56*(2), 339–355. https://doi.org/10.1016/j.neuron.2007.09.017

Pnevmatikakis, E. A., Soudry, D., Gao, Y., Machado, T. A., Merel, J., Pfau, D., … Paninski, L. (2016). Simultaneous Denoising, Deconvolution, and Demixing of Calcium Imaging Data. *Neuron*, *89*(2), 285–299. https://doi.org/10.1016/j.neuron.2015.11.037

Polley, D. B., Read, H. L., Storace, D. A., & Merzenich, M. M. (2007). Multiparametric Auditory Receptive Field Organization Across Five Cortical Fields in the Albino Rat. *Journal of Neurophysiology*, *97*(5), 3621–3638. https://doi.org/10.1152/jn.01298.2006

Rakic, P. (1976). Prenatal genesis of connections subserving. *Nature*, *26*.

Rakic, P., Ayoub, A. E., Breunig, J. J., & Dominguez, M. H. (2009). Decision by division: making cortical maps. *Trends in Neurosciences*, *32*(5), 291–301. https://doi.org/10.1016/j.tins.2009.01.007

Rochefort, N. L., Garaschuk, O., Milos, R.-I., Narushima, M., Marandi, N., Pichler, B., … Konnerth, A. (2009). Sparsification of neuronal activity in the visual cortex at eye-opening. *Proceedings of the National Academy of Sciences of the*

United States of America, *106*(35), 15049–15054. https://doi.org/10.1073/pnas.0907660106

Rochefort, N. L., Narushima, M., Grienberger, C., Marandi, N., Hill, D. N., & Konnerth, A. (2011). Development of direction selectivity in mouse cortical neurons. *Neuron*, *71*(3), 425–432. https://doi.org/10.1016/j.neuron.2011.06.013

Sanderson, M. J., Smith, I., Parker, I., & Bootman, M. D. (2014). Fluorescence Microscopy Michael. *Cold Spring Harbor Protocols*, *10*(10), 1–36. https://doi.org/10.1101/pdb.top071795.Fluorescence

Sasaki, T., Takahashi, N., Matsuki, N., & Ikegaya, Y. (2008). Fast and Accurate Detection of Action Potentials From Somatic Calcium Fluctuations. *Journal of Neurophysiology*, *100*(3), 1668–1676. https://doi.org/10.1152/jn.00084.2008

Schreiber, T. (2000). Measuring information transfer. *Physical Review Letters*, *85*(2), 461–464. https://doi.org/10.1103/PhysRevLett.85.461

Seelke, A. M. H., Karlsson, K. A., Gall, A. J., & Blumberg, M. S. (2005). Extraocular muscle activity, rapid eye movements and the development of active and quiet sleep. *European Journal of Neuroscience*, *22*(4), 911–920. https://doi.org/10.1111/j.1460-9568.2005.04322.x

Siegel, F., Heimel, J. A., Peters, J., & Lohmann, C. (2012). Peripheral and central inputs shape network dynamics in the developing visual cortex in vivo. *Current Biology*, *22*(3), 253–258. https://doi.org/10.1016/j.cub.2011.12.026

Smith, G. B., Hein, B., Whitney, D. E., Fitzpatrick, D., & Kaschube, M. (2018). Distributed network interactions and their emergence in developing neocortex. *Nature Neuroscience*, *21*(November), Kaschub. https://doi.org/10.1038/s41593-018-0247-5

Smith, S. L., & Trachtenberg, J. T. (2007). Experience-dependent binocular competition in the visual cortex begins at eye opening. *Nature Neuroscience*,

10(3), 370–375. https://doi.org/10.1038/nn1844

Smith, S. M. (2012). The future of FMRI connectivity. *NeuroImage*. https://doi.org/10.1016/j.neuroimage.2012.01.022

Smith, S. M., Miller, K. L., Salimi-Khorshidi, G., Webster, M., Beckmann, C. F., Nichols, T. E., … Woolrich, M. W. (2011). Network modelling methods for FMRI. *NeuroImage*. https://doi.org/10.1016/j.neuroimage.2010.08.063

Son, A. I., Fu, X., Suto, F., Liu, J. S., Hashimoto-Torii, K., & Torii, M. (2017). Proteome dynamics during postnatal mouse corpus callosum development. *Scientific Reports*. https://doi.org/10.1038/srep45359

Song, D. (2013). *Identification of Sparse Neural Functional Connectivity using Penalized Likelihood Estimation and Basis Functions*. *PLoS ONE* (Vol. 32). https://doi.org/10.1371/journal.pone.0178059

Sonntag, M., Englitz, B., Kopp-Scheinpflug, C., & Rubsamen, R. (2009). Early Postnatal Development of Spontaneous and Acoustically Evoked Discharge Activity of Principal Cells of the Medial Nucleus of the Trapezoid Body: An In Vivo Study in Mice. *Journal of Neuroscience*, *29*(30), 9510–9520. https://doi.org/10.1523/jneurosci.1377-09.2009

Spitzer, N. C. (2006). Electrical activity in early neuronal development. *Nature*, *444*(7120), 707–712. https://doi.org/10.1038/nature05300

Steinmetz, N. A., Buetfering, C., Lecoq, J., Lee, C. R., Peters, A. J., Jacobs, E. A. K., … Harris, K. D. (2017). Aberrant Cortical Activity in Multiple GCaMP6-Expressing Transgenic Mouse Lines. *Eneuro*, *4*(5), ENEURO.0207-17.2017. https://doi.org/10.1523/ENEURO.0207-17.2017

Sutera, A., Joly, A., François-Lavet, V., Qiu, Z. A., Louppe, G., Ernst, D., & Geurts, P. (2014). Simple connectome inference from partial correlation statistics in calcium imaging, 23–35. Retrieved from http://arxiv.org/abs/1406.7865

Tagawa, Y., & Hirano, T. (2012). Activity-dependent callosal axon projections in neonatal mouse cerebral cortex. *Neural Plasticity*, *2012*. https://doi.org/10.1155/2012/797295

Tau, G. Z., & Peterson, B. S. (2010). Normal development of brain circuits. *Neuropsychopharmacology*, *35*(1), 147–168. https://doi.org/10.1038/npp.2009.115

Theis, L., Berens, P., Froudarakis, E., Reimer, J., Román Rosón, M., Baden, T., … Bethge, M. (2016). Benchmarking Spike Rate Inference in Population Calcium Imaging. *Neuron*, *90*(3), 471–482. https://doi.org/10.1016/j.neuron.2016.04.014

Thévenaz, P., Ruttimann, U. E., & Unser, M. (1998). A Pyramid Approach to Sub-Pixel Registration Based on Intensity Mailing address. *IEEE Transactions on Image Processing*, *7*(1), 27–41. https://doi.org/10.1109/83.650848

Tierney, A. L., & Nelson, C. A. (2009). Brain Development and the Role of Experience in the Early Years. *Zero to Three*, *30*(2), 9–13. Retrieved from http://www.ncbi.nlm.nih.gov/pubmed/23894221%0Ahttp://www.pubmedcentral.nih.gov/articlerender.fcgi?artid=PMC3722610

Tiriac, A., Del Rio-Bermudez, C., & Blumberg, M. S. (2014). Self-generated movements with “unexpected” sensory consequences. *Current Biology*, *24*(18), 2136–2141. https://doi.org/10.1016/j.cub.2014.07.053

Tiriac, A., Uitermarkt, B. D., Fanning, A. S., Sokoloff, G., & Blumberg, M. S. (2012). Rapid whisker movements in sleeping newborn rats. *Current Biology*, *22*(21), 2075–2080. https://doi.org/10.1016/j.cub.2012.09.009

Tkacik, G., Mora, T., Marre, O., Amodei, D., Berry, M. J., & Bialek, W. (2014). Thermodynamics for a network of neurons: Signatures of criticality, *112*(37), 11508–11513. https://doi.org/10.1073/pnas.1514188112

Tolner, E. A., Sheikh, A., Yukin, A. Y., Kaila, K., & Kanold, P. O. (2012). Subplate

Neurons Promote Spindle Bursts and Thalamocortical Patterning in the Neonatal Rat Somatosensory Cortex. *Journal of Neuroscience*, *32*(2), 692–702. https://doi.org/10.1523/JNEUROSCI.1538-11.2012

Triplett, J. W., Owens, M. T., Yamada, J., Lemke, G., Cang, J., Stryker, M. P., & Feldheim, D. A. (2009). Retinal Input Instructs Alignment of Visual Topographic Maps. *Cell*, *139*(1), 175–185. https://doi.org/10.1016/j.cell.2009.08.028

Tritsch, N. X., Yi, E., Gale, J. E., Glowatzki, E., & Bergles, D. E. (2007). The origin of spontaneous activity in the developing auditory system. *Nature*. https://doi.org/10.1038/nature06233

Vann, S. D., Aggleton, J. P., & Maguire, E. A. (2009). What does the retrosplenial cortex do? *Nature Reviews Neuroscience*, *10*(11), 792–802. https://doi.org/10.1038/nrn2733

Vanni, M. P., Chan, A. W., Balbi, M., Silasi, G., & Murphy, T. H. (2017). Mesoscale Mapping of Mouse Cortex Reveals Frequency-Dependent Cycling between Distinct Macroscale Functional Modules. *The Journal of Neuroscience*, *37*(31), 7513–7533. https://doi.org/10.1523/JNEUROSCI.3560-16.2017

Veeriah, V., Durvasula, R., & Qi, G.-J. (2015). Deep Learning Architecture with Dynamically Programmed Layers for Brain Connectome Prediction, 1205–1214. https://doi.org/10.1145/2783258.2783399

Villette, V., Guigue, P., Picardo, M. A., Sousa, V. H., Leprince, E., Lachamp, P., … Baude, A. (2016). Development of early-born ??-Aminobutyric acid hub neurons in mouse hippocampus from embryogenesis to adulthood. *Journal of Comparative Neurology*, *524*(12), 2440–2461. https://doi.org/10.1002/cne.23961

Vogelstein, J. T., Packer, A. M., Machado, T. A., Sippy, T., Babadi, B., Yuste, R., & Paninski, L. (2010). Fast non-negative deconvolution for spike train inference

from population calcium imaging, 1–26. https://doi.org/10.1152/jn.01073.2009

Wang, H. C., Lin, C. C., Cheung, R., Zhang-Hooks, Y., Agarwal, A., Ellis-Davies, G., … Bergles, D. E. (2015). Spontaneous Activity of Cochlear Hair Cells Triggered by Fluid Secretion Mechanism in Adjacent Support Cells. *Cell*, *163*(6), 1348–1359. https://doi.org/10.1016/j.cell.2015.10.070

Yamawaki, N., Radulovic, J., & Shepherd, G. M. G. (2016). A Corticocortical Circuit Directly Links Retrosplenial Cortex to M2 in the Mouse. *The Journal of Neuroscience*, *36*(36), 9365–9374. https://doi.org/10.1523/JNEUROSCI.1099-16.2016

Yang, J.-W., Hanganu-Opatz, I. L., Sun, J.-J., & Luhmann, H. J. (2009). Three Patterns of Oscillatory Activity Differentially Synchronize Developing Neocortical Networks In Vivo. *Journal of Neuroscience*, *29*(28), 9011–9025. https://doi.org/10.1523/JNEUROSCI.5646-08.2009

Yang, J. W., An, S., Sun, J. J., Reyes-Puerta, V., Kindler, J., Berger, T., … Luhmann, H. J. (2013). Thalamic network oscillations synchronize ontogenetic columns in the newborn rat barrel cortex. *Cerebral Cortex*, *23*(6). https://doi.org/10.1093/cercor/bhs103

YEHEZKEL BEN-ARI, ENRICO CHERUBINI, R. C. A. J.-L. G. (1989). GIANT SYNAPTIC POTENTIALS IN IMMATURE RAT CA3 HIPPOCAMPAL NEURONES, *5*, 303–325.

YingXin Zhang-Hooks, Amit Agarwal, Masayoshi Mishina, & Dwight E. Bergles. (2016). NMDA Receptors Enhance Spontaneous Activity and Promote Neuronal Survival in the Developing Cochlea YingXin. *Neuron*, *118*(24), 6072–6078. https://doi.org/10.1002/cncr.27633.Percutaneous

Yuste, R., Nelson, D. A., Rubin, W. W., & Katz, L. C. (1995). Neuronal domains in developing neocortex: Mechanisms of coactivation. *Neuron*, *14*(1), 7–17.

https://doi.org/10.1016/0896-6273(95)90236-8

Zucker, R. S. (1999). Calcium- and activity-dependent synaptic plasticity. *Current Opinion in Neurobiology*, *9*(3), 305–313. https://doi.org/10.1016/S0959-4388(99)80045-2

Statement of Contributions

This dissertation study was carried out in the Institute of Physiology, Department of Neurophysiology, at the Eberhard Karls Universität Tübingen under the supervision of Professor Dr. Olga Garaschuk. This work was conceived by Professor Dr. Olga Garaschuk.

Setup design and preparation was performed by Dr. Yury Kovalchuk and all experiments in this study were performed by me and Dr. Yury Kovalchuk.

Analyses toolbox design and implementation and all data analyses were performed by me.

I wrote this dissertation under the supervision of Professor Dr. Olga Garaschuk.

Curriculum vitae

Education / Employment

- Ph.D., Computational Neuroscience 2015-2019
  Eberhard Karls University of Tübingen
  Dissertation: Stable behavioral state-specific meso-scale activity patterns in the developing cortex of neonates
  Supervisor: Prof. Dr. Olga Garaschuk
- Master of Science, Electrical Eng. & Information Technology 2011-2014
  Otto-von-Guericke university of Magdeburg
  Thesis: Information transfer in neurophysiological data
  Supervisor: Prof. Dr.-Ing. Hermann Hinrichs
- Data Analyst 2013-2014
  Leibniz Institute of Neurobiology Magdeburg
- Software Developer Intern 2012-2013
  Philips Healthcare, Best, Eindhoven
- Bachelor's degree, Electronic Eng. 2006-2010
  Azad university of Tabriz

Publications

- **Mojtahedi N**., Kovalchuk Y., Böttcher A., Garaschuk O. Stable behavioral state-specific mesoscale activity patterns in the developing cortex of neonates(*manuscript in preparation*).
- Lerdkrai C., Asavapanumas N., Brawek B., Kovalchuk Y., **Mojtahedi N.**, Olmedillas-del-Moral M.,Garaschuk O. Intracellular Ca2+ stores control in vivo neuronal hyperactivity in a mouse model of Alzheimer's disease. Proc. Natl. Acad. Sci. U. S. A. (2018). doi:10.1073/pnas.1714409115
- Riester K., Brawek B., Asavapanumas N., **Mojtahedi N.**, Garaschuk O. Mechanisms of cortical hyperactivity induces by systemic inflammation *in vivo* (*manuscript in preparation*).
- Riester K., Brawek B., Savitska D., Fröhlich N., Zirdum E., **Mojtahedi N.**, Heneka M., Garaschuk O. In vivo characterization of functional states of cortical microglia during peripheral inflammation (*manuscript in preparation*).